

# Non-adiabatic tidal forcing of a massive, uniformly rotating star II: The low frequency, inertial regime

G.J. Savonije<sup>1</sup> and J.C. Papaloizou<sup>2</sup>

<sup>1</sup> *Astronomical Institute ‘Anton Pannekoek’, University of Amsterdam and Centre for High Energy Astrophysics (CHEAF), Kruislaan 403, 1098 SJ Amsterdam, The Netherlands*

<sup>2</sup> *Astronomy Unit, School of Mathematical Sciences, Queen Mary & Westfield College, Mile End Road, London E1 4NS*

3 December 2017

## ABSTRACT

We study the fully non-adiabatic tidal response of a uniformly rotating unevolved  $20M_{\odot}$  star to the dominant  $l = m = 2$  component of the companion’s perturbing potential. This is done numerically with a 2D implicit finite difference scheme. We assume the star is rotating slowly with angular speed  $\Omega_s \ll \Omega_c$ , so that the centrifugal force can be neglected, but the Coriolis force is taken fully into account. We study the low frequency ‘inertial’ regime  $|\bar{\sigma}| < 2\Omega_s$ , where  $\bar{\sigma}$  is the forcing frequency in the frame rotating with the stellar spin rate  $\Omega_s$ . In this frequency range inertial modes are excited in the convective core which can interact with rotationally modified g- or r-modes in the radiative envelope and cause significant strengthening of the tidal interaction. Resonant interaction with quasi-toroidal (r-)modes in slightly super-synchronous stars causes efficient spin down towards corotation. We determine timescales for tidal spin-up and spin-down in the inertial frequency regime for stars spinning with  $\Omega_s = 0.1\Omega_c$  and  $0.2\Omega_c$ .

**Key words:** Hydrodynamics– Stars: binaries– Stars: rotation– Stars: oscillation – Stars: tides

## 1 INTRODUCTION

In a series of earlier papers we studied the tidal response of an early type star in a close binary system (e.g. a massive X-ray binary), ignoring stellar rotation, but taking into account the effects of internal nuclear evolution (Savonije & Papaloizou 1983, 1984: SP83, SP84 and Papaloizou & Savonije 1985: PS85). Recently, we extended these studies by taking into account the effects of the Coriolis force in uniformly rotating stars (Savonije, Papaloizou & Alberts 1995: SPA95). We found that, as expected, in a rotating star resonances between the  $l = 2$  tide and internal modes are possible not only for  $l = 2$ , but also with modes with predominantly  $l = 4$  or  $l = 6$  etc. due to the mode coupling by the Coriolis force. Once the relative forcing frequency  $\bar{\sigma}$  was smaller than twice the stellar rotation speed, however, the numerical results were swamped by short wavelength inertial waves. We could only study the (positive frequency range of the) inertial regime by adopting the so called ‘traditional approximation’ in which the  $\theta$ -part of the stellar angular speed  $\Omega_s$  is ignored. It appeared that rotationally modified g-modes continued to be excited in this frequency range but that for  $\bar{\sigma} < \Omega_s$ , no reliable results could be obtained. Therefore a new implicit 2D scheme was developed that is numerically more stable and that can treat three-level difference equations, enabling viscosity to be introduced in the equations of motion. The viscosity can then be used to damp the shortest wavelength inertial waves. We have used this new scheme to explore the inertial regime, introducing a much finer grid resolution in the radial direction. For free oscillations, the low frequency inertial regime was studied by e.g. Berthomieu et al. (1978), Saio (1982) and by Lee & Saio (1987, 1989). However, these authors did not take the Coriolis force fully into account, but used the ‘traditional approximation’, or truncated (to the first few terms) the infinite expansion in spherical harmonics required to describe the oscillations in rotating stars. We take the Coriolis force fully into account, by not using spherical harmonics expansions, but solving the full 2D problem in  $r$  and  $\theta$ . Also we consider (tidally) forced oscillations. The next section (2) summarizes our basic equations, followed by a brief section (3) on the stellar input model. Then, in section 4, we present our numerical results. In the appendix we list the finite difference approximation to the partial differential equations describing

non-radial oscillations that give stable numerical results and a short description of the new implicit 2D elimination scheme used to solve these equations.

## 2 BASIC EQUATIONS

We consider a uniformly rotating, early type secondary star with mass  $M_s$  and radius  $R_s$  in a close binary with circular orbit with angular velocity  $\omega$  and orbital separation  $D$ . We assume the secondary's angular velocity of rotation  $\vec{\Omega}_s$  to be much smaller than its break-up speed, i.e.  $(\Omega_s/\Omega_c)^2 \ll 1$ , with  $\Omega_c^2 = GM_s/R_s^3$ , so that effects of centrifugal distortion ( $\propto \Omega_s^2$ ) may be neglected in first approximation. We wish to study the response of this uniformly rotating star to a perturbing time-dependent tidal force. The Coriolis acceleration is proportional to  $\Omega_s$  and we consider its effect on the tidally induced motions in the star. We use spherical coordinates  $(r, \theta, \varphi)$ , with origin at the secondary's centre, whereby  $\theta = 0$  corresponds to its rotation axis which we assume to be parallel to the orbital angular momentum vector. We take the coordinates to be non-rotating.

As is well known, in a non-rotating star the solutions of the linearized non-radial stellar oscillation equations can be expressed in terms of spherical harmonics, i.e. the spatial part of each mode can be fully separated into  $r$ -,  $\theta$ - and  $\varphi$ -factors (e.g. Ledoux & Walraven 1958)

$$U(r, \theta, \varphi) = u(r)P_l^m(\cos\theta)e^{im\varphi},$$

where  $P_l^m$  represents the associated Legendre polynomials for  $l$  and  $|m|$ .

The introduction of the Coriolis force, however, destroys the full separability of the oscillation equations, it only being retained for the  $\varphi$ -dependence. It turns out (e.g. Berthomieu, Gonczi, Graff, Provost & Rocca 1978) that two independent sets of approximately spheroidal oscillation modes exist: modes in which the density perturbation is *even* with respect to reflection in the equatorial plane, which have  $l - |m|$  even valued, and modes with *odd* symmetry for the density, having  $l - |m|$  odd valued. In addition, for each  $l$ , there is a set of approximately toroidal modes (e.g. Papaloizou & Pringle 1978) which couple with the spheroidal modes of  $l \pm 1$ .

Let us denote perturbed Eulerian quantities like pressure  $P'$ , density  $\rho'$ , temperature  $T'$  and energy flux  $\mathbf{F}'$  with a prime. The linearized hydrodynamic equations governing the non-adiabatic response of the uniformly rotating star to the perturbing potential  $\Phi_T$  may then be written

$$\left[ \left( \frac{\partial}{\partial t} + \Omega_s \frac{\partial}{\partial \varphi} \right) v_i \right] \mathbf{e}_i + 2\Omega_s \mathbf{k} \times \mathbf{v}' = -\frac{1}{\rho} \nabla P' + \frac{\rho'}{\rho^2} \nabla P - \nabla \Phi_T, \quad (1)$$

$$\left( \frac{\partial}{\partial t} + \Omega_s \frac{\partial}{\partial \varphi} \right) \rho' + \nabla \cdot (\rho \mathbf{v}') = 0, \quad (2)$$

$$\left( \frac{\partial}{\partial t} + \Omega_s \frac{\partial}{\partial \varphi} \right) [S' + \mathbf{v}' \cdot \nabla S] = -\frac{1}{\rho T} \nabla \cdot \mathbf{F}', \quad (3)$$

$$\frac{\mathbf{F}'}{F} = \left( \frac{dT}{dr} \right)^{-1} \left[ \left( \frac{3T'}{T} - \frac{\rho'}{\rho} - \frac{\kappa'}{\kappa} \right) \nabla T + \nabla T' \right]. \quad (4)$$

where  $\mathbf{e}_i$  are the unit vectors of our spherical coordinate system,  $\mathbf{k}$  is the unit vector along the rotation axis,  $\mathbf{v}'$  denotes the velocity perturbation,  $\kappa$  the opacity of stellar material and  $S$  its specific entropy. These perturbation equations represent, respectively, conservation of momentum, conservation of mass and conservation of energy, while the last equation describes the radiative diffusion of the perturbed energy flux. For simplicity we adopt the Cowling (1941) approximation, i.e. we neglect perturbations to the gravitational potential caused by the secondary's distortion. We also neglect perturbations of the nuclear energy sources and of convection.

The dominant tidal term of the primary's perturbing potential is given by the real part of

$$\Phi_T(r, \theta, \varphi, t) = fr^2 P_2^2(\mu) e^{2i(\omega t - \varphi)} \quad (5)$$

where  $\mu = \cos\theta$ ,  $P_2^2(\mu)$  is the associated Legendre polynomial for  $l = |m| = 2$  and  $f = -\frac{GM_p}{4D^3}$ , with  $M_p$  the companion's mass. Adopting the same azimuthal  $m = 2$  symmetry and time dependence for the perturbed quantities as the forcing potential, the perturbed velocity  $\mathbf{v}' = 2i(\omega - \Omega_s)\xi$ , where  $\xi$  is the displacement vector. The perturbations can be written as e.g.

$$\xi_r(r, \theta, \varphi, t) = \hat{\xi}_r(r, \theta) e^{2i(\omega t - \varphi)}$$

where  $\xi_r$  is the radial component of the displacement vector and  $\hat{\xi}_r(r, \theta)$  is assumed complex to describe the phase shift  $\Delta\varphi$  with respect to the forcing potential (5).

For numerical reasons it proved better not to eliminate  $\xi_\varphi$  from the equations, as was done in SPA95, and retain the  $\varphi$ -equation of motion. However, we do eliminate  $F'_\varphi$  with help of the  $\varphi$ -component of the radiative transport equation. Writing

for simplicity from now on  $\xi_r$  for  $\widehat{\xi}_r(r, \theta)$  etc., while dividing out the factor  $e^{2i(\omega t - \varphi)}$ , equations (1)–(4) transform into the equations (6)–(12) given below.

The radial equation of motion becomes

$$\rho \bar{\sigma}^2 \xi_r + [2i\bar{\sigma}\Omega_s \sin \theta \rho] \xi_\varphi - \frac{\partial}{\partial r} \left( P \chi_\rho \frac{\rho'}{\rho} \right) - \frac{\partial}{\partial r} \left( P \chi_T \frac{T'}{T} \right) + \frac{dP}{dr} \left( \frac{\rho'}{\rho} \right) - 6f\rho r (\sin \theta)^2 = 0 \quad (6)$$

where  $\bar{\sigma} = 2\bar{\omega} \equiv 2(\omega - \Omega_s)$  is the forcing frequency felt by a mass element in the uniformly rotating secondary, while  $\chi_\rho = \frac{\partial}{\partial \ln \rho} \ln P$  and  $\chi_T = \frac{\partial}{\partial \ln T} \ln P$  follow from the equation of state.

The  $\theta$ -equation of motion becomes

$$\rho \bar{\sigma}^2 \xi_\theta + [2i\bar{\sigma}\Omega_s \cos \theta \rho] \xi_\varphi - \left( \frac{P \chi_\rho}{r} \right) \frac{\partial}{\partial \theta} \left( \frac{\rho'}{\rho} \right) + - \left( \frac{P \chi_T}{r} \right) \frac{\partial}{\partial \theta} \left( \frac{T'}{T} \right) - 6f\rho r \sin \theta \cos \theta = 0 \quad (7)$$

The  $\varphi$ -equation of motion becomes

$$\rho \bar{\sigma}^2 \xi_\varphi - [2i\bar{\sigma}\Omega_s \sin \theta \rho] \xi_r - [2i\bar{\sigma}\Omega_s \cos \theta \rho] \xi_\theta + \left[ \frac{imP\chi_\rho}{r \sin \theta} \right] \left( \frac{\rho'}{\rho} \right) + \left[ \frac{imP\chi_T}{r \sin \theta} \right] \left( \frac{T'}{T} \right) + 3imf\rho r \sin \theta = 0 \quad (8)$$

The perturbed equation of continuity is transformed into

$$\frac{\rho'}{\rho} + \frac{1}{r^2 \rho} \frac{\partial}{\partial r} (r^2 \rho \xi_r) + \frac{1}{r \sin \theta} \frac{\partial}{\partial \theta} (\sin \theta \xi_\theta) - \frac{im}{r \sin \theta} \xi_\varphi = 0 \quad (9)$$

By applying the thermodynamic relation

$$\delta S = S' + \xi \cdot \nabla S = \frac{P}{\rho T} \frac{1}{\Gamma_3 - 1} \left( \frac{\delta P}{P} - \Gamma_1 \frac{\delta \rho}{\rho} \right)$$

where the symbol  $\delta$  denotes a Lagrangian perturbation and  $\Gamma_j$  the adiabatic exponents of Chandrasekhar, the perturbed energy equation can be transformed into

$$\begin{aligned} & \left[ \frac{d \ln P}{dr} - \Gamma_1 \frac{d \ln \rho}{dr} \right] \xi_r + [\chi_\rho - \Gamma_1] \left( \frac{\rho'}{\rho} \right) + \left[ \chi_T + i\eta \left( \frac{m}{r \sin \theta} \right)^2 \left( \frac{d \ln T}{dr} \right)^{-1} \right] \left( \frac{T'}{T} \right) + \\ & -i\eta \left[ \frac{1}{r^2} \frac{\partial}{\partial r} \left( r^2 \frac{F'_r}{F} \right) + \frac{d \ln F}{dr} \left( \frac{F'_r}{F} \right) \right] + +i\eta \left[ \frac{\sin \theta}{r} \frac{\partial}{\partial \mu} \left( \frac{F'_\theta}{F} \right) - \frac{\cos \theta}{r \sin \theta} \left( \frac{F'_\theta}{F} \right) \right] = 0 \end{aligned} \quad (10)$$

where

$$\eta = (\Gamma_3 - 1) \frac{F}{\bar{\sigma} P}$$

is a local characteristic radiative diffusion length in the star, with  $F$  the unperturbed (radial) energy flux. When  $\eta \rightarrow 0$  the response becomes adiabatic and shows (outside resonance) no phase shift with respect to the companion. However, even for ‘high’ frequencies  $\bar{\sigma}/\Omega_c \approx 1$  the diffusion length  $\eta$  becomes comparable to the scale height when the stellar surface is approached, so that the imaginary part of the surface response becomes comparable to the real part.

The perturbed radial energy flux is given by

$$\left( \frac{F'_r}{F} \right) = \left( \frac{d \ln T}{dr} \right)^{-1} \frac{\partial}{\partial r} \left( \frac{T'}{T} \right) + - (\kappa_T - 4) \left( \frac{T'}{T} \right) - (\kappa_\rho + 1) \left( \frac{\rho'}{\rho} \right) \quad (11)$$

where  $\kappa_\rho = \frac{\partial}{\partial \ln \rho} \ln \kappa$  and  $\kappa_T = \frac{\partial}{\partial \ln T} \ln \kappa$ . Finally the  $\theta$ -component of the perturbed flux follows as

$$\left( \frac{F'_\theta}{F} \right) = - \frac{\sin \theta}{r} \left( \frac{d \ln T}{dr} \right)^{-1} \frac{\partial}{\partial \mu} \left( \frac{T'}{T} \right). \quad (12)$$

where  $\mu = \cos \theta$ .

## 2.1 Boundary conditions

The differential equations are supplemented by the following boundary conditions: at the stellar centre we require  $\xi_r$  and  $F'_r$  to vanish, while at the stellar surface, we require the Lagrangian pressure perturbations to vanish

$$\frac{P'}{P} + \frac{d \ln P}{dr} \xi_r = 0 \quad (13)$$

and the temperature and flux perturbations to fulfill Stefan–Boltzmann’s law

$$\frac{F'_r}{F} = \left( \frac{2}{r} + 4 \frac{d \ln T}{dr} \right) \xi_r + 4 \left( \frac{T'}{T} \right). \quad (14)$$

Furthermore,  $\xi_\theta$  and  $F'_\theta$  must vanish on the rotation axis while in view of the symmetry of the tidal force we adopt mirror symmetry about the equatorial plane, i.e., for  $\theta = \pi/2$  we also require  $\xi_\theta$  and  $F'_\theta$  to vanish.

## 2.2 Viscous damping of short wavelength response in convective regions

In order to damp the short wavelength (of order gridsizes) response to the tidal forcing in the inertial regime in the non-stratified (convective) regions of the star, viscous terms are added to the equations of motion. We use a simple mixing length prescription for both energy transport and turbulent viscosity in convective regions. We adopt a (constant) reduction factor  $\epsilon$  for the turbulent viscosity to roughly take into account the mismatch between the forcing time and the convective timescale in the core. The turbulent viscosity  $\zeta$  can thus be expressed as

$$\zeta = \epsilon H_P \left( \frac{F}{10\rho} \right)^{\frac{1}{3}} \quad (15)$$

where  $F$  is the local energy flux and  $H_P$  the local pressure scale height. For the turbulent viscosity in the convective core a reduction factor  $\epsilon = 10^{-3}$  is adopted (adequate to damp the grid oscillations for all applied forcing frequencies), while in the convective outer shell a slightly larger value  $\epsilon = 3 \times 10^{-2}$  had to be taken. At the boundary of the convective regions we let the viscosity  $\zeta$  drop to negligible values as  $\exp\left[-\left(\frac{2d}{H_P}\right)^2\right]$ , where  $d$  is the distance from the boundary. Fig. 1 shows the adopted  $\zeta$  distribution through the star. A significant steeper decline to zero viscosity at the convective core boundary would not prevent the short wavelength inertial response to penetrate into the weakly stratified regions adjacent to the core. Adopting a much steeper decline (decline on scale  $0.1H_P$ ) changed the tidal torque by less than a few percent. In the convective surface shell near  $i \simeq 1600$ , the ratio of the forcing time to the local viscous time  $\tau_v = \frac{\Delta r^2}{\zeta}$  (where  $\Delta r$  is the local gridsizes) becomes larger than unity. But since the mass in these layers is negligible this has no effect on the tidal torque, which is predominantly applied in the radiative region adjacent to the convective core.

With this prescription for the viscosity in the convective regions the grid oscillations are adequately damped while the global numerical results, like the tidal torque, appear insensitive to the adopted viscosity. Only if  $\zeta$  is taken some orders of magnitude larger do the global numerical results like the net tidal torque change significantly.

The (simplified) viscous terms that are added to the equations of motion are expressed in such a way that the PDE's (6)-(7) retain their separability in  $r$  and  $\theta$  when  $\Omega_s \rightarrow 0$ .

The radial equation of motion (6) is extended with the following viscous terms

$$i\bar{\sigma} \frac{\rho\zeta}{r^2} \left[ (1 - \mu^2) \frac{\partial^2}{\partial \mu^2} \xi_r - 2\mu \frac{\partial}{\partial \mu} \xi_r - \frac{4}{1 - \mu^2} \xi_r \right] + \frac{i\bar{\sigma}}{r^2} \frac{\partial}{\partial r} \left( \rho\zeta r^2 \frac{\partial \xi_r}{\partial r} \right) \quad (16)$$

while to the  $\theta$ -equation of motion the following terms are added

$$i\bar{\sigma} \frac{\rho\zeta}{r^2} \left[ (1 - \mu^2) \frac{\partial^2}{\partial \mu^2} \xi_\theta - 4\mu \frac{\partial}{\partial \mu} \xi_\theta - \frac{5 - 2\mu^2}{1 - \mu^2} \xi_\theta \right] + \frac{i\bar{\sigma}}{r^2} \frac{\partial}{\partial r} \left( \rho\zeta r^2 \frac{\partial \xi_\theta}{\partial r} \right) \quad (17)$$

## 3 THE UNPERTURBED STELLAR MODEL

A recent version (Pols, Tout, Eggleton & Han 1995) of the stellar evolution code developed by Eggleton (1972) was used to construct the unperturbed stellar input model for the secondary. The model represents a spherical zero-age main-sequence star of  $20 M_\odot$  with chemical composition  $X = 0.70$  and  $Z = 0.02$ . The model was constructed with the OPAL opacities (Iglesias & Rogers 1993). With these opacities the  $20 M_\odot$  ZAMS star appears to have shallow convection zones in the envelope which are absent when the Cox–Stewart opacities are used. The stellar radius equals  $R_s = 4.993 \times 10^{11}$  cm, while the stellar moment of inertia  $I_s = 7.21 \times 10^{56}$  g cm<sup>2</sup>. The break-up angular speed equals  $\Omega_c = 1.46 \times 10^{-4}$  s<sup>-1</sup>. In the convective core, which has a mass of about  $10 M_\odot$ , the imaginary Brunt–Väisälä frequency  $\mathcal{A}^{\frac{1}{2}}$  given by

$$\mathcal{A} = \frac{1}{\rho} \frac{dP}{dr} \left( \frac{1}{\rho} \frac{d\rho}{dr} - \frac{1}{\gamma P} \frac{dP}{dr} \right). \quad (18)$$

reaches a maximum value of about  $|\mathcal{A}|^{\frac{1}{2}} = 5 \times 10^{-3} \ll \Omega_s$ , where  $|\mathcal{A}|^{\frac{1}{2}}$  is given in units of  $\Omega_c$ , while in the outer convective shell  $|\mathcal{A}|^{\frac{1}{2}} \simeq 5$ , see Fig. 1. This corresponds to a super-adiabaticity  $\nabla - \nabla_{ad} \simeq 10^{-6}$  and 0.07 in the core and envelope shell, respectively.

It can be seen that the radial grid has about 500 zones in the convective core, about 600 zones in the adjacent radiative ‘plateau region’ where the eigenfunctions of g- and r-modes have most of their radial nodes, and also several hundred zones in the rarified outer layers with convective shells.

## Stellar input model

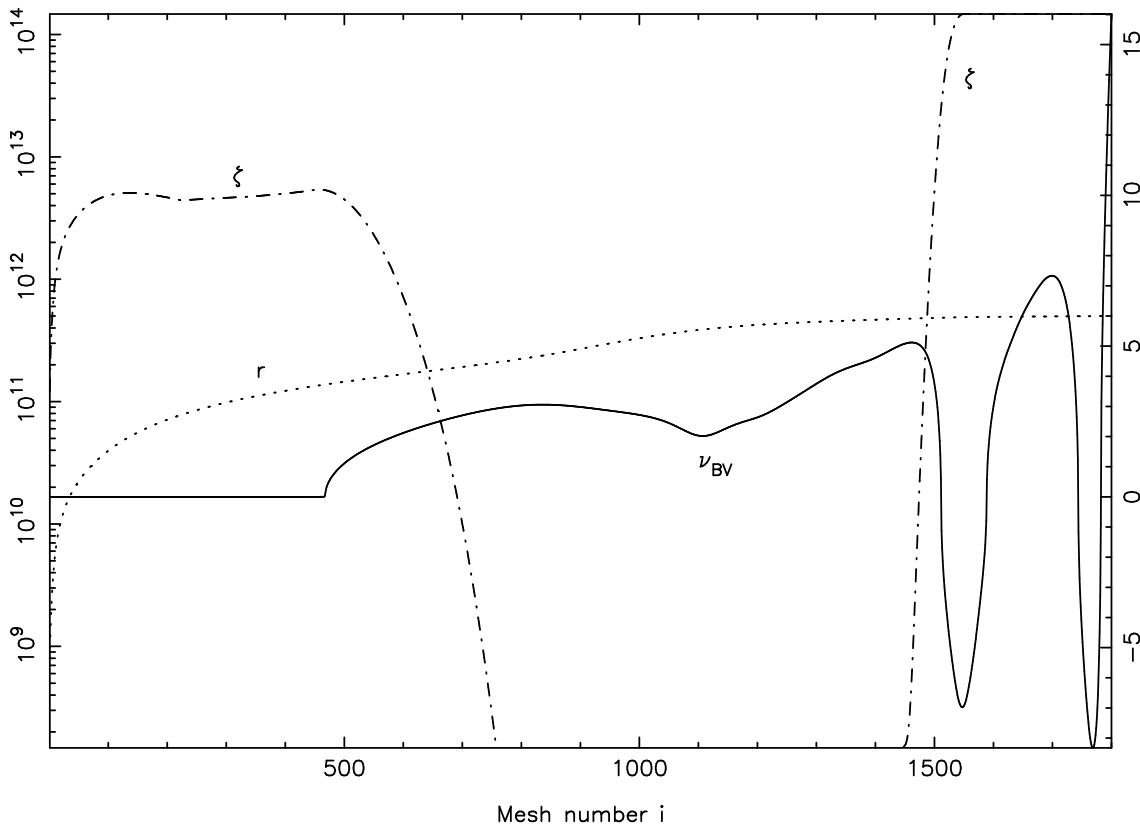


**Figure 1.** Characteristics of the  $20 M_{\odot}$  stellar input model: the (adapted) Brunt–Väisälä frequency  $\nu_{\text{BV}} = \text{sign} \mathcal{A} \sqrt{|\mathcal{A}|}$  in units of the stellar break-up speed  $\Omega_c$  (vertical scale on the right), radius  $r$  in cm and turbulent viscosity  $\zeta$  in cgs units (vertical scale on the left) as a function of radial mesh number.

### 3.1 Non-adiabatic surface layer (NASL)

A crude random walk estimate for the time required for heat to diffuse to the stellar surface from a given point  $r$  in the stellar envelope is given by

$$\tau_{th} = \frac{\rho \kappa (R_s - r)^2 \beta}{c(1 - \beta)}$$

where  $\kappa$  is the opacity,  $c$  the velocity of light, and  $\beta$  the ratio of gas to total pressure. By comparing this timescale with the forcing time  $\tau_f = 2\pi/\bar{\sigma}$ , we find that non-adiabatic effects become important ( $\tau_{th} \simeq \tau_f$ ) roughly from radial zone 1300 (for  $\bar{\omega} = 0.01\Omega_c$ ) or 1400 (for  $\bar{\omega} = 0.20\Omega_c$ ) outwards. The convective shells are thus located in this thin non-adiabatic layer, see Fig. 1, so that the (adiabatic) Brunt–Väisälä frequency  $|\mathcal{A}|^{\frac{1}{2}}$  greatly overestimates the convective growth rate there ( $\tau_{th}^{-1} \simeq 3\Omega_c$  in the innermost convective shell). Also the thermal stratification in the radiative part of the non-adiabatic layer is much weaker than suggested by the large values  $|\mathcal{A}|^{\frac{1}{2}} \simeq 5\Omega_c$  or even higher, attained in that region.

## 4 NUMERICAL RESULTS

### 4.1 Introduction

We extend the calculations of SPA95 into the low-frequency inertial regime, i.e. for forcing frequencies  $|\bar{\sigma}| < 2\Omega_s$ . In SPA95 the numerical results in this frequency regime were swamped by short wavelength inertial waves in the convective core, which also propagated into the weakly stratified radiative regions adjacent to the core, unless we adopted the ‘traditional approximation’ in which the  $\theta$  component of the stellar angular velocity  $\Omega_s$  is neglected. And even then, we could not obtain reliable results for  $\bar{\omega} < 0.1$ , where  $\bar{\omega} = \frac{1}{2}\bar{\sigma}$  is the tidal pattern speed in the corotating frame expressed in units of  $\Omega_c$ . From now on we shall express all frequencies in units of  $\Omega_c = (GM_s/R_s^3)^{\frac{1}{2}}$ .

Equations (6)-(12) have been approximated by the set of finite difference equations (FDE’s) (A1-A7) given in the appendix.

The FDE's with appropriate boundary conditions are then solved by a newly developed 2D implicit elimination scheme briefly explained in appendix B. With this new three-level finite difference scheme we can effectively damp the very short (gridsize) inertial waves by introducing a modest (turbulent) viscosity  $\zeta$  in the equations of motion, see equations (16) -(17).

## 4.2 Fourier-Legendre coefficients

For each forcing frequency  $\bar{\sigma}$  the calculated stellar response can be expanded in Fourier-Legendre (FL) series with complex coefficients  $C_l^m(r)$ , e.g.

$$\xi_r(r, \mu) = \sum_{l=0}^{\infty} C_l^m(r) P_l^m(\mu)$$

with

$$C_l^m(r) = \frac{(2l+1)(l-m)!}{2(l+m)!} \int_{-1}^1 \xi_r(r, \mu) P_l^m(\mu) d\mu.$$

By plotting the real and imaginary parts of  $C_l^m(r)$  for the various perturbed variables versus  $r$  for  $m = 2$  and different  $l$ -values, we can compare the strength of the different  $l$ -components in the response.

## 4.3 Tidal response in non-rotating stars

To compare our results for (uniformly) rotating stars with those of non-rotating stars we have recalculated (for  $\omega < 0.1$ ) the tidal response for a non-rotating star with the same 2-D scheme and with the same viscosity. For forcing frequencies in the range considered here the amplitude of the displacement vector  $\xi$  globally follows that of the equilibrium tide, except that in the subsurface layers ( $i > 1500$ ), a peak occurs which grows with decreasing tidal frequency  $\sigma = 2\omega$ . For  $\omega = 0.025$  the radial displacement peaks at more than twice the value of the equilibrium tide near  $i = 1500$ , while  $\xi_r$  decreases to the equilibrium value near the stellar surface. The  $\theta$ -displacement is generally an order of magnitude larger than  $\xi_r$  near the surface. The mass in the NASL is only small, so that the effect on the total torque is generally insignificant. The likely reason for this strong sub-surface response is that for low forcing frequencies the radiative losses in the surface layers (section 3.1) get so strong that the characteristic timescale for convective oscillatory motions becomes comparable to the forcing period. Indeed, when a zero value for the radiative diffusion length  $\eta$  (adiabatic calculation) is adopted the strong sub-surface response disappears.

## 4.4 Tidal response in sub-synchronous stars ( $\Omega_s < \omega$ )

For sub-synchronously rotating ( $\bar{\omega} > 0$ ) early type stars rotationally modified g-modes are excited in the radiative envelope for all frequencies in the inertial regime, down to near co-rotation. The g-modes have a predominant  $l = 2$  component, with  $l = 4$  and 6 components having in general a factor 4-10 weaker amplitudes in this frequency range. If the relative forcing frequency  $\bar{\sigma} = 2\bar{\omega} = 2(\omega - \Omega_s)$  in the frame corotating with the secondary falls below  $2\Omega_s$ , inertial waves are excited in the weakly or non-stratified layers. Once  $\bar{\omega} < \Omega_s$  the first signs of inertial waves are observed, not only in the convective core, but even stronger in the non-adiabatic surface layer (NASL) containing the convective shells (section 3.1). Without viscosity the tidal response in the convective regions gets overwhelmed by short lengthscale (gridsize) variations, as discussed in SPA95. The excitation of inertial modes in the core is discussed in section 4.7.

As discussed above for non-rotating stars, the strong radiative damping in the NASL gives rise to large amplitude oscillatory convective motion in the sub-surface layers. With rotation the non-adiabatic response in the sub-surface layers shows even larger  $\theta$ -displacements, while the response is more complex with high  $l$ -components due to inertial effects.

Fig. 2 shows an example of the  $\theta$ -dependence of the tidal response in the sub-surface layers of a star rotating with  $\Omega_s = 0.1$  for a forcing frequency  $\bar{\omega} = 0.076$ . At  $i = 1400$  (not shown) the  $\theta$  dependence is still typically that of the radiative region outside the convective core and consists predominantly of a simple  $l = 2$  ( $\xi_r$ ) or  $l = 3$  ( $\xi_\theta$ ) component. The displacement  $\xi_\theta/R_s$  attains a maximum of about  $8 \times 10^{-4}$  at  $i = 1400$ . However, slightly further out (from about  $i = 1500$ ) inertial waves are excited which show up as short wavelength oscillations. The amplitude of the displacement vector  $\xi$  shows a peak at around  $\cos \theta \simeq \bar{\omega}/\Omega_s$  with an oscillatory decay towards the rotation axis. Note that g-modes become evanescent when the oscillation frequency is smaller than twice the average radial component of the stellar angular velocity  $2\Omega_s \cos \theta$  (e.g. Eckart 1960), so that the peak amplitude of the tidal response appears to coincide roughly with the turning point of those modes. Inertial waves can propagate from pole to equator.

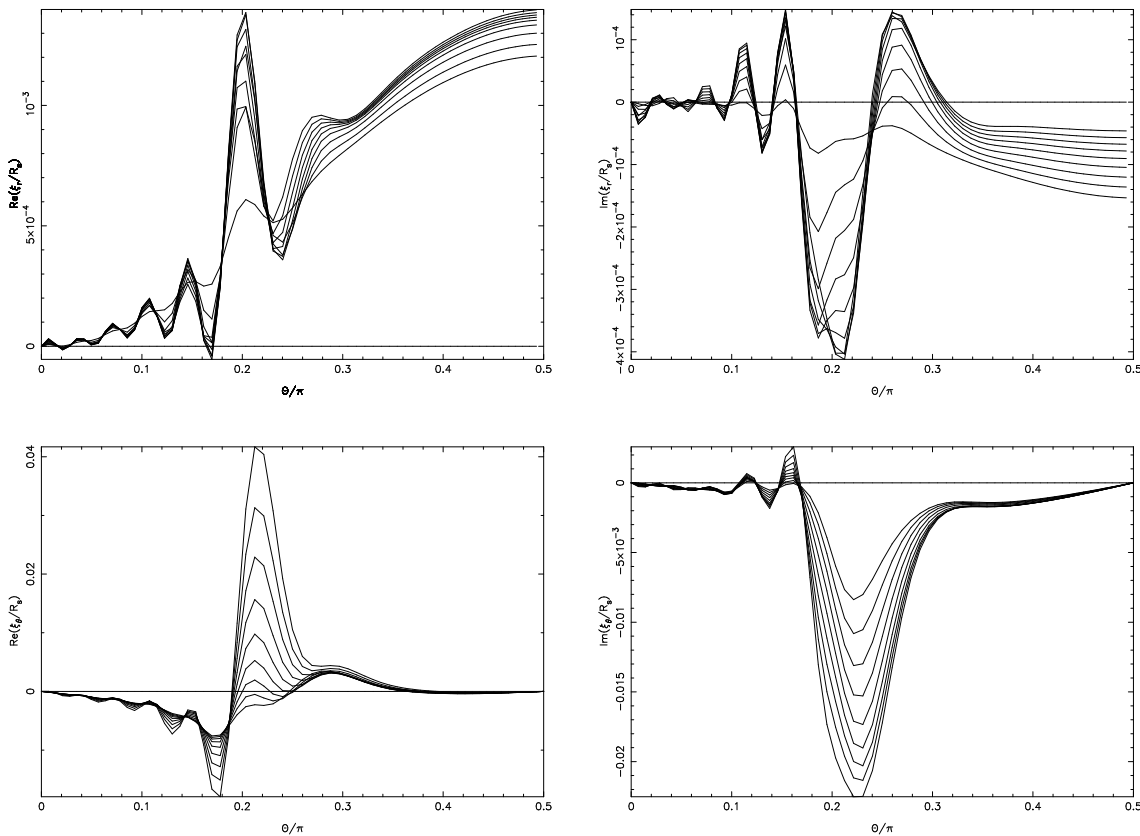


**Figure 2.**  $\bar{\omega} = 0.076$  and  $\Omega_s = 0.1$ : the  $\theta$ -dependence of the radial- and  $\theta$ -component of the displacement vector for radial zones in the range  $i = 1650 - 1750$ , corresponding to  $r/R_s = 0.992 - 0.998$ , i.e. in between the two convective shells near the surface. The left hand panels give the real parts, the right hand panels the imaginary parts. The shortest lengthscales were removed by viscous damping.

#### 4.5 Tidal response in super-synchronous stars ( $\Omega_s > \omega$ )

When we lower the forcing frequency - through corotation to negative values - the tidal response becomes qualitatively different. Now the excited tidal wave becomes retrograde as the star is spinning faster than the orbital revolution of its companion. For small  $|\bar{\omega}|$  there are again many radial nodes in the radiative envelope, as there are for small positive frequencies, but now the displacements show a strong toroidal component. When  $|\bar{\omega}|$  is increased a rapid succession of strong resonances occurs, these are resonances with free r-modes, e.g. Papaloizou and Pringle 1978, Provost, Berthomieu & Rocca (1981), Rocca (1982) and SPA95, analogous to Rossby-waves in the earth's atmosphere (e.g. Pedlosky 1977). Because the excited r-modes occupy only a small frequency range approximately given by  $-\frac{m\Omega_s}{l(l+1)} < \bar{\omega} < 0$  with  $l = 3$  and  $m = 2$ , strong resonances with low order (with few radial nodes in the envelope) r-modes are possible for relatively small  $|\bar{\omega}|$ , i.e. close to corotation.

Hence, in contrast to early type *sub*-synchronous stars approaching corotation, which tend to spin up towards corotation as a result of weak resonances with high-order, strongly damped g-modes, slightly *super*-synchronous stars tend to spin down towards corotation much more efficiently due to strong resonances with weakly damped r-modes (see Figs. 8-9).

Figs. 3 shows the radial distribution of the dominant FL-coefficients of the radial and  $\theta$ -displacement for the strong resonance at  $\bar{\omega} = -0.0166$  with the lowest order r-mode that could be found for a star rotating at  $\Omega_s = 0.1$ . In the radiative envelope the radial displacement is typically three orders of magnitude smaller than the  $\theta$ -displacement which shows the (quasi-)toroidal character of this mode.

For this low order r-mode resonance,  $|\xi|$  attains values large compared to the equilibrium tide (Fig. 3) not only in the radiative envelope, but also in the convective core. The response in the core is oscillatory, both in  $r$  and  $\theta$  (Fig. 4) indicating the excitation of an inertial core mode. Fig. 5 shows the  $\theta$ -dependence of the radial and  $\theta$  displacement in the convective shell region.

When  $\bar{\omega}$  is made more negative than  $\bar{\omega} \simeq -\frac{m\Omega_s}{l(l+1)}$  the imaginary parts of the perturbed quantities decrease substantially. The imaginary part of  $\rho'$  shows weak oscillations in the core and envelope, with an evanescent zone in between (from about  $i=700$  to  $i=1100$ ). At the boundary of the convective core a (relatively) strong spike occurs. When  $\bar{\omega}$  is made more negative, a very short wavelength response appears just outside this spike, which starts to extend outwards, grow in amplitude, and fill up the 'evanescent' region. At  $\bar{\omega} = -0.0375$  (for  $\Omega_s = 0.1$ ) some 80 radial nodes occur in the radiative envelope. It appears that,

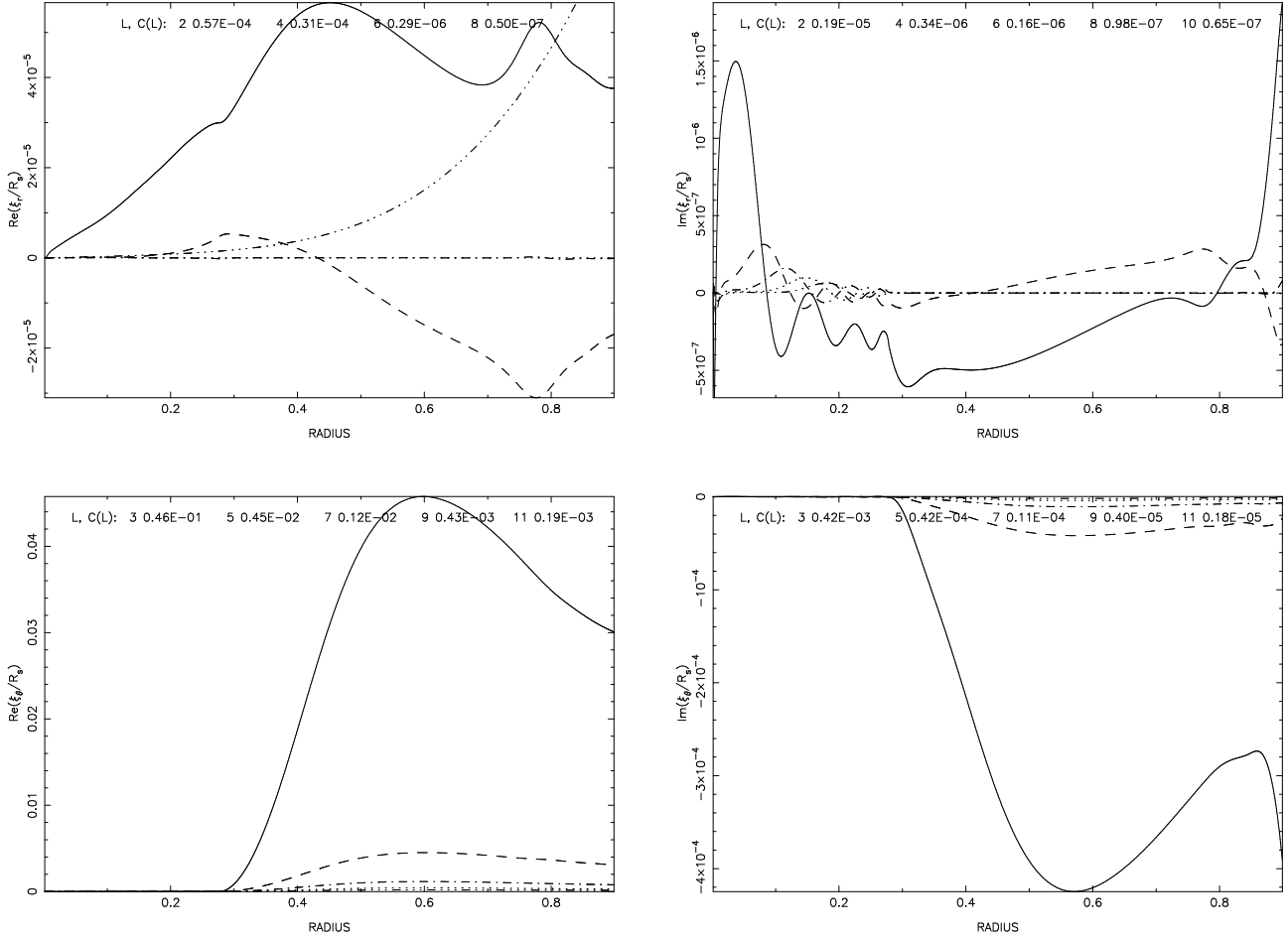


**Figure 3.**  $\bar{\omega} = -0.0166$  and  $\Omega_s = 0.1$ : corresponding to a stellar rotation period of  $P_s = 5.0$  days and orbital period  $P_b \simeq 6$  days. Plotted are the dominant Fourier-Legendre coefficients versus radius for the radial and  $\theta$ -displacement for the lowest order resonance with an  $r$ -mode. The various curves correspond to the consecutive  $l$ -values shown inside each panel (from left  $l$ -value to right  $l$ -value: full line, dashed line, dot-dash, dotted and dash-dot-dot-dot). The real number  $C(l)$  given after each  $l$ -value is the maximum value attained over the star for that particular FL-coefficient. In the  $\xi_r$  panel the dash-dot-dot-dot line gives the corresponding amplitude of the equilibrium tide. The surface layers ( $i > 1300$ ) have been cut away in order to see the smaller amplitude structure of  $\text{Im}(\xi_r)$  in the interior.

by decreasing the forcing frequency, a transition has been made from the  $r$ -modes to the rotationally modified, retrograde  $g$ -modes. For more negative frequencies the number of radial nodes decreases and we proceed through resonances with lower and lower order  $g$ -modes, until the limit  $\bar{\omega} = -\Omega_s$  is approached when  $\omega \rightarrow 0$ .



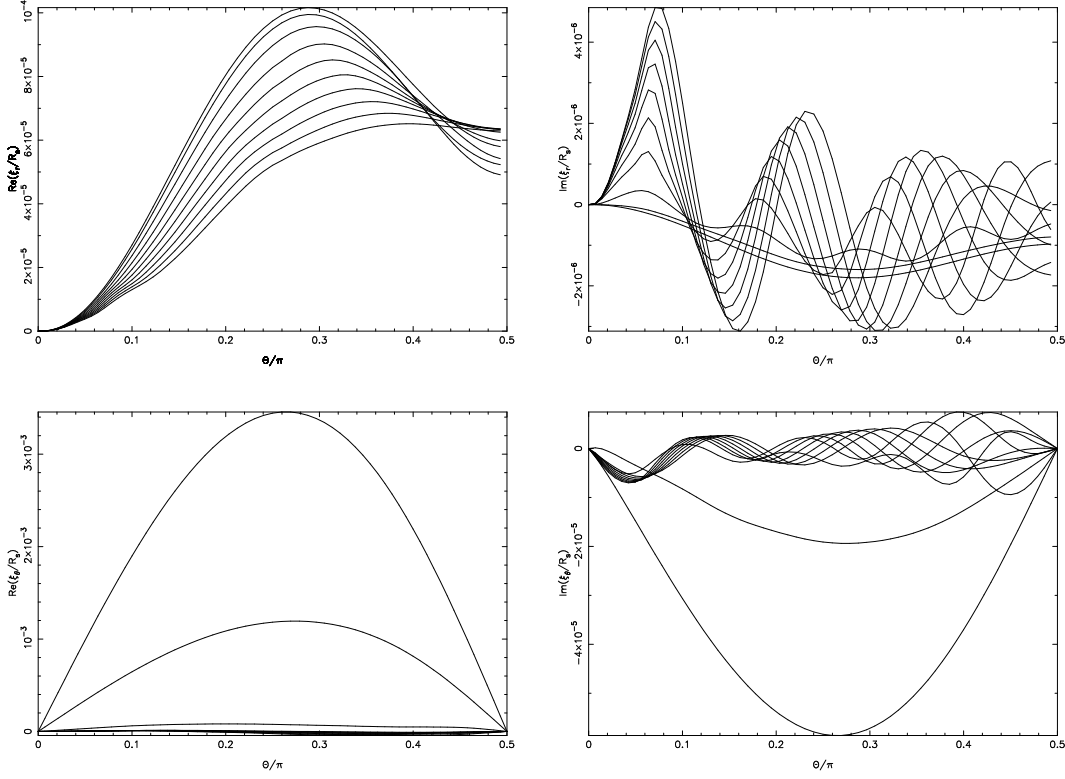


**Figure 4.**  $\bar{\omega} = -0.0166$  and  $\Omega_s = 0.1$ : the radial and  $\theta$  displacement in the outer part of the convective core (radial zones in the range  $i = 350 - 450$ ) as a function of  $\theta$ . The real parts show the predominant  $l = 2$  ( $\xi_r$ ) and  $l = 3$  ( $\xi_\theta$ ) dependency on  $\theta$ , while the oscillatory imaginary parts indicate the excitation of inertial waves. The shortest lengthscales were damped by viscosity.

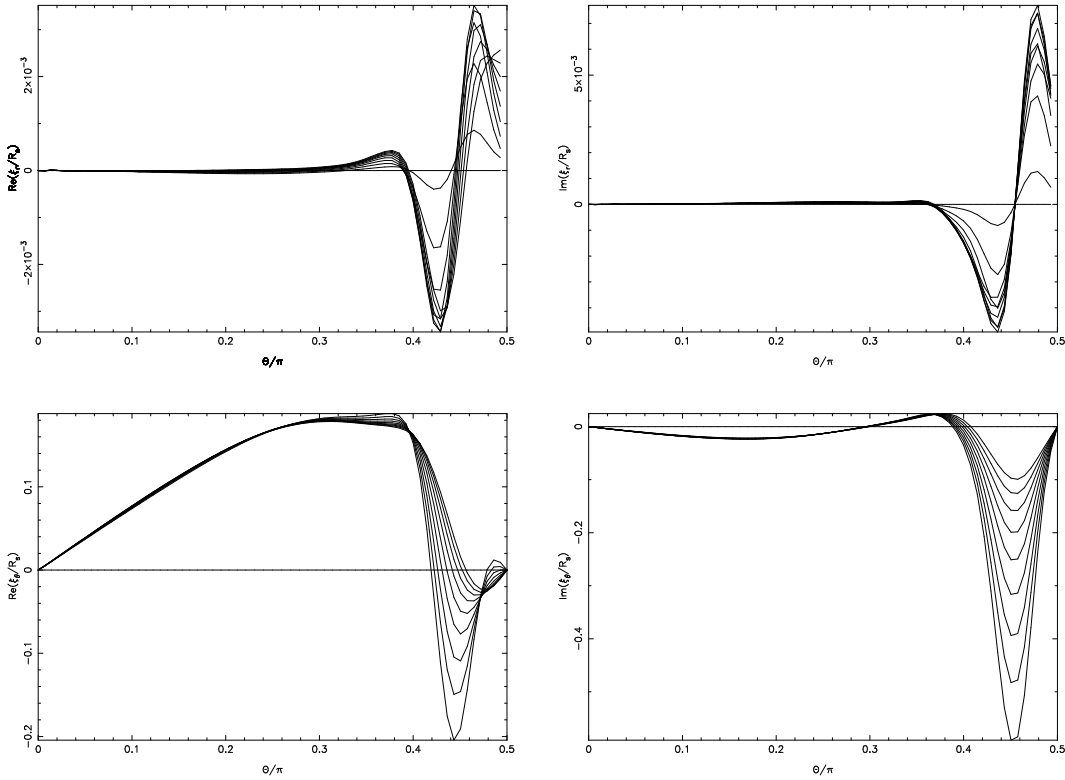


**Figure 5.**  $\bar{\omega} = -0.0166$  and  $\Omega_s = 0.1$ : the radial and  $\theta$  displacement in the region between the two convective surface shells ( $i = 1650 - 1750$ ) as a function of  $\theta$ .

$$\Omega_s = 0.10 \quad \omega - \Omega_s = 0.0185 \quad t_0 = 0.411\text{E}+02 \text{ yr} \quad \text{Torque} = 0.127\text{E}+37 \text{ cgs}$$

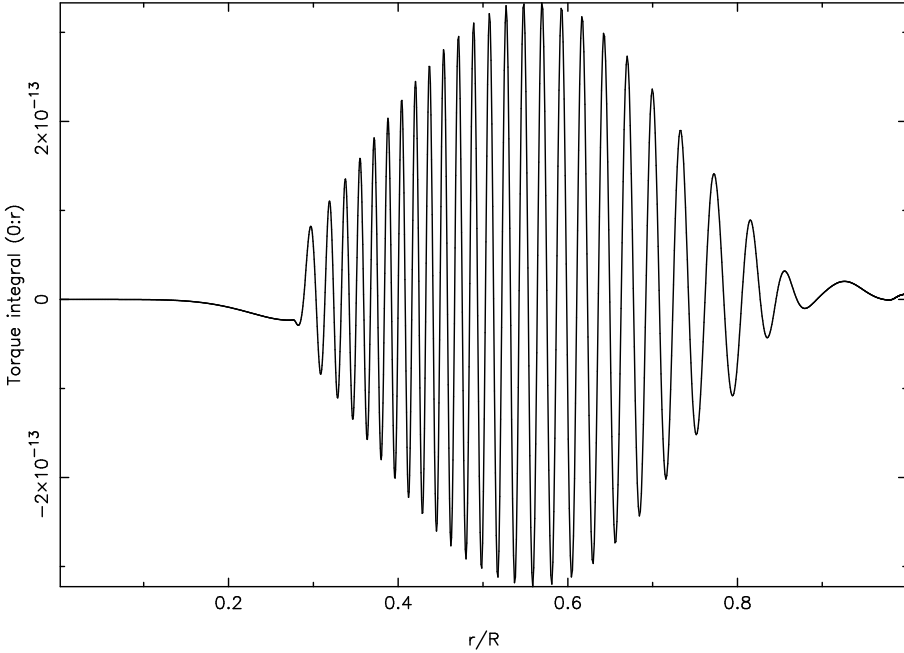


**Figure 6.** The torque integral (19) integrated from 0 to  $r$  as a function of  $r$  for  $\bar{\omega} = 0.0185$  and  $\Omega_s = 0.1$ . This forcing frequency corresponds to a strong resonance with an inertial mode in the core, causing a broad dip in the  $t_0$  curve, see Fig. 8. The values of the plotted torque integral are given in units of  $GM_s^2/R_s$ .

#### 4.6 Tidal torque and stellar spin-up/down time

The radiative damping in the surface layers of tidally excited non-radial oscillation modes introduces a phase shift between the mode and the forcing potential. This phase shift gives rise to a net tidal torque on the secondary

$$\mathcal{T}_{\text{ext}} = 2\pi f \int_0^{R_s} \int_{-1}^1 \text{Im}(\rho') r^4 P_2^2(\mu) dr d\mu \quad (19)$$

When the secondary rotates slower than synchronously ( $\Omega_s < \omega$ ) the net torque is positive and give rise to a spin up, while for super-synchronous stars ( $\Omega_s > \omega$ ) the tidal wave is retrograde in the frame co-rotating with the secondary and yield a negative tidal torque, leading to spin down.

The secondary's spin-up/down time-scale  $t_{\text{sp}}$  follows as

$$t_{\text{sp}}^{-1} = \frac{\mathcal{T}_{\text{ext}}}{I_s \bar{\omega}}$$

where  $I_s$  is the secondary's moment of inertia. Let us now define, as in our earlier studies, the 'intrinsic' spin-up time  $t_0$  of the secondary as

$$t_0(\bar{\omega}) = \left(\frac{M_p}{M_s}\right)^2 \left(\frac{R_s}{D}\right)^6 t_{\text{sp}}(\bar{\omega}). \quad (20)$$

in which we have divided out the dependency of the  $l = m = 2$  forcing on the specific binary configuration.

By varying the forcing frequency  $\bar{\sigma} = 2\bar{\omega}$  and calculating the tidal torque according to equation (19) we can determine the 'intrinsic' tidal spin-up time  $t_0$  (equation 20) as a function of  $\bar{\omega}$ .

Fig. 7 shows the calculated  $t_0$  distribution for a non-rotating star, whereby the numbers along the curve indicate the number of radial nodes of the tidal oscillations. The dotted curve corresponds to a low-frequency approximation (PS85):

$$t_0(\omega) = \frac{k}{\Omega_c} \left(\frac{M_{cc}}{M_s}\right)^{\frac{4}{3}} \left(\frac{R_{cc}}{R_s}\right)^{-9} \left(\frac{\omega}{\Omega_c}\right)^{-\frac{5}{3}} \quad (21)$$

where  $k$  is the star's gyration radius ( $I_s = kM_s R_s^2$ ) and  $R_{cc}$ ,  $M_{cc}$  are the radius and mass of the convective core. This expression is based on a simple model which assumes a purely adiabatic star with a thin very non-adiabatic outer shell, so that all outward propagating gravity waves are absorbed by radiative damping in the outer shell. Expression (21) is similar to that obtained by Zahn (1977) and is valid only for non-rotating unevolved massive stars in the limit of low forcing frequencies.

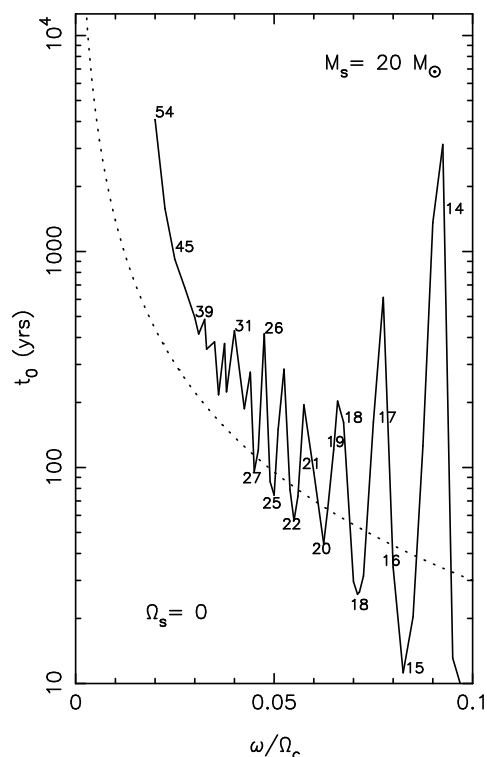


**Figure 7.** The scaled spin-up or spin-down time  $t_0$  versus  $\bar{\omega}$  for a non-rotating  $20 M_\odot$  star. For comparison the low frequency limit (21) is also plotted (dotted curve). The number of radial nodes is indicated along the curve.

In Papaloizou & Savonije 1997 (PS97) the asymptotic low frequency expression for  $t_0$  is generalized to include the effects of stellar rotation.

Figs. 8 and 9 show the calculated intrinsic spin-up or down time  $t_0(\bar{\omega})$  versus tidal frequency for a  $20 M_\odot$  star rotating at a rate  $\Omega_s = 0.1$  and  $\Omega_s = 0.2$ , respectively. For low frequency  $g$ -modes, which have many radial nodes, a strong cancellation effect occurs whereby the torque integral, when integrated over the envelope, changes sign many times. This can be seen in Fig. 6 where the torque integral (19), integrated from  $r = 0$  to  $r$ , is plotted versus  $r$  for the response at  $\bar{\omega} = 0.0185$ . At this frequency a strong resonance occurs with an inertial mode in the core, see next section. Meshpoints 1500-1800 (the convective shell region) correspond to  $r/R > 0.98$ . Note that for small positive values of the forcing frequency the wavelength of  $g$ -modes in the envelope becomes too small ( $> 50$  radial nodes) for adequate resolution on the grid.

For rotating stars which can have negative forcing frequencies when the star spins faster than the orbital revolution of its companion, the  $t_0$  curve has an extra branch for  $\bar{\omega} < 0$ . Rotational effects make the  $t_0$  curve qualitatively different, not only for the new branch with  $\bar{\omega} < 0$ , but also for  $\bar{\omega} > 0$ . The Coriolis force couples modes with even  $l$ - values, so that  $l = 2$  forcing indirectly excites  $l = 4, 6 \dots$  as well. It also gives rise to a frequency shift of the non-radial oscillations. Comparing Figs. 7 and 8 shows that, as expected, a shift to lower eigen-frequencies has occurred in the rotating star (e.g. Ledoux & Walraven 1958, SPA95). The response for negative forcing frequencies is distinctly different from that for positive frequencies. For small negative forcing frequencies resonances with free rotationally controlled (quasi-)toroidal r-modes show up as strong narrow dips in the  $t_0$  curve. These strong resonances can cause a rapid spin-down of slightly super-synchronous stars. For more negative forcing frequencies once again resonances with (retrograde, rotationally modified)  $g$ -modes become possible. The more negative forcing frequencies correspond to lower order resonances (with fewer radial nodes) that are damped only weakly, with consequently smaller  $t_0$  values.

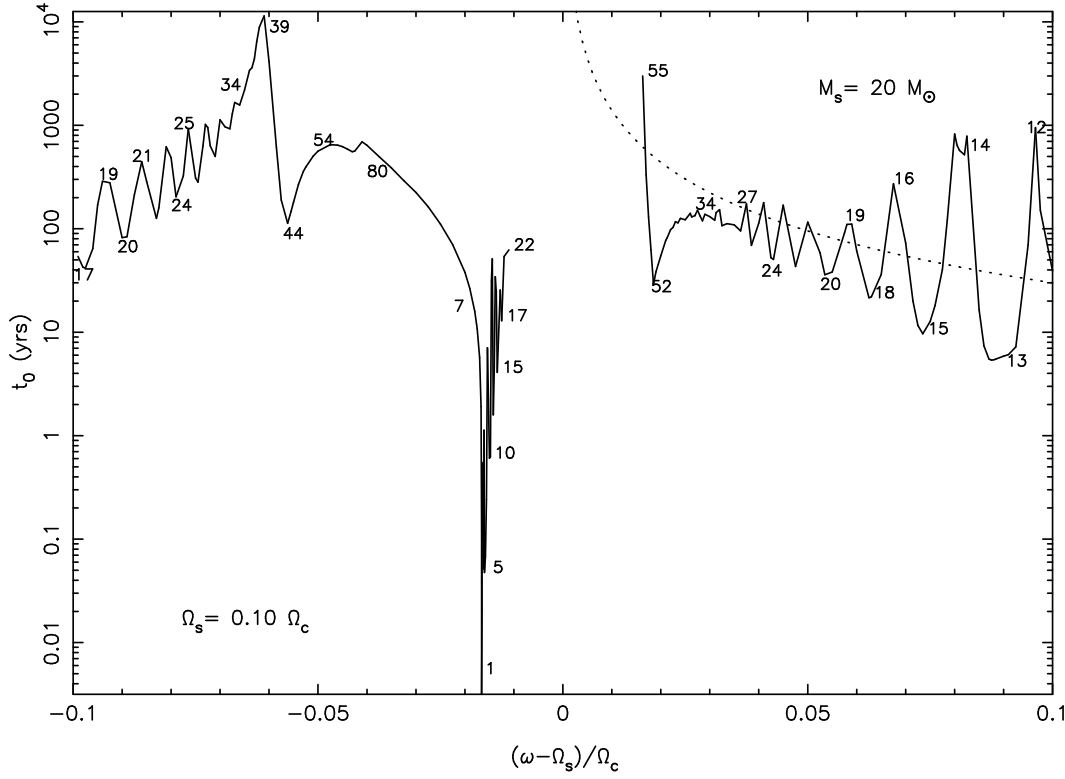


**Figure 8.** The scaled spin-up or spin-down time  $t_0$  versus  $\bar{\omega}$  for a uniformly rotating  $20 M_{\odot}$  star at a rate  $\Omega_s = 0.1$ . The number of radial nodes in the envelope is indicated along the curve. For comparison the low frequency limit (21), whereby we have simply replaced  $\omega$  by  $\bar{\omega}$ , is also plotted (dotted curve).

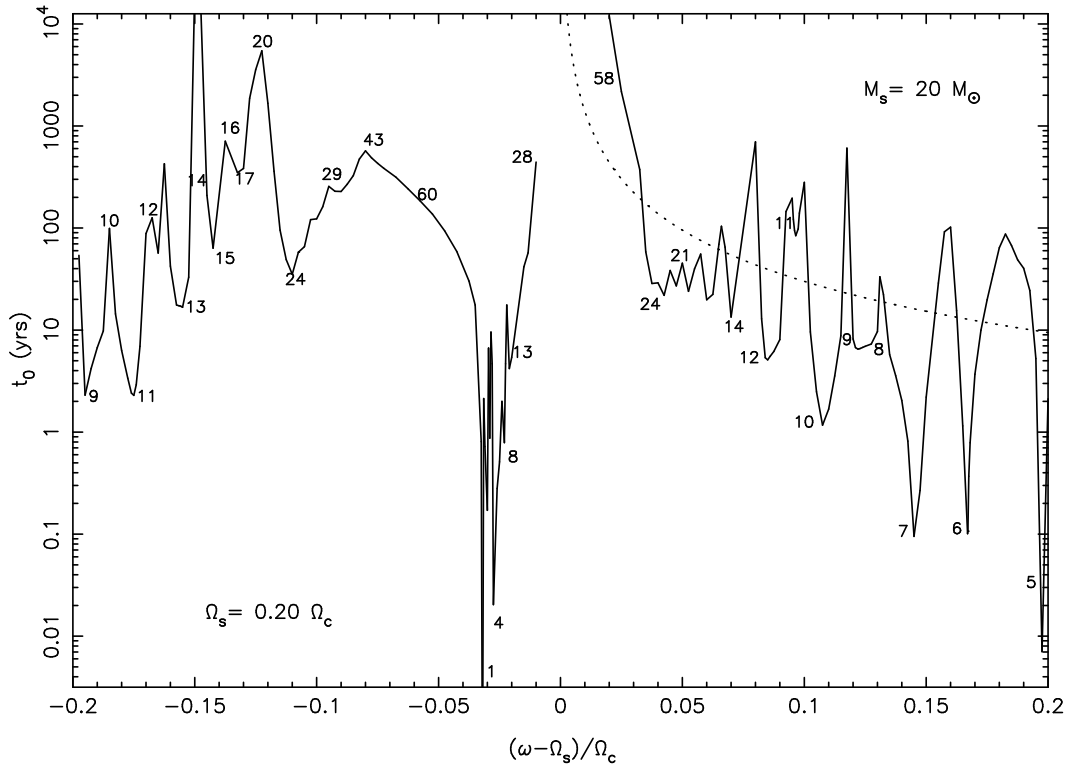


**Figure 9.** The scaled spin-up or spin-down time  $t_0$  versus  $\bar{\omega}$  for a uniformly rotating  $20 M_{\odot}$  star at a rate  $\Omega_s = 0.2$ . The number of radial nodes in the envelope is indicated along the curve. For comparison the low frequency limit (21), whereby we have simply replaced  $\omega$  by  $\bar{\omega}$ , is also plotted (dotted curve).

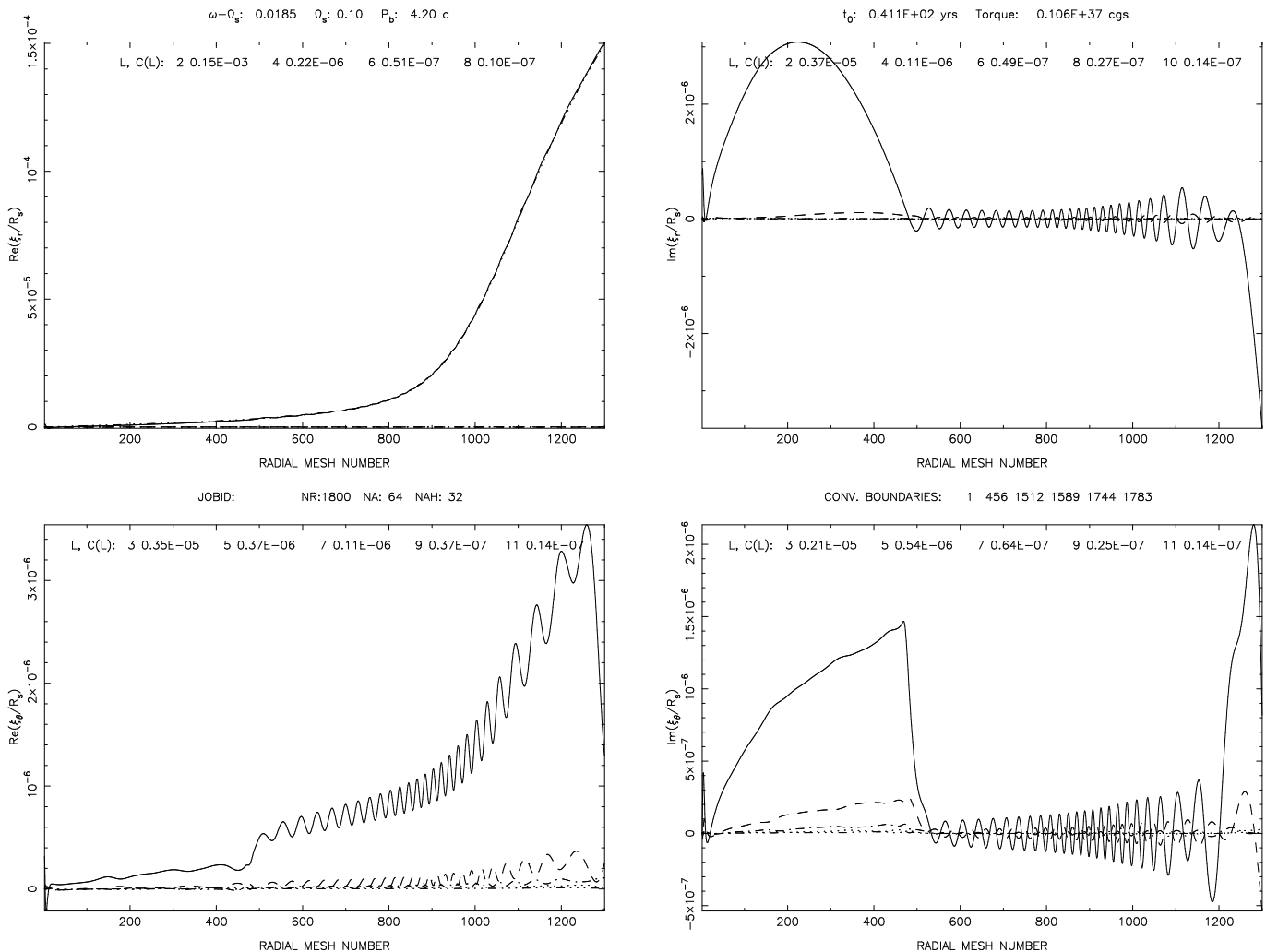


**Figure 10.** The dominant FL-coefficients for the radial and  $\theta$  displacement versus radius for the tidal response at  $\bar{\omega} = 0.0185$  and  $\Omega_s = 0.1$  (similar to figure 3). For this forcing frequency the tide is resonant with an inertial mode in the convective core. The convective core boundary is at  $i \simeq 460$ . The non-adiabatic surface layer, where the amplitude becomes large, is not shown.

#### 4.7 Excitation of inertial modes in the convective core

Although the inertial modes have a dense spectrum their amplitude under tidal forcing remains limited. This is probably partly due to coupling with envelope modes which keeps the amplitude down because of leaking. However, the long scale tidal force is not efficient in exciting inertial modes. For a constant density and pressure core it can be shown (PS97) that only two potential inertial mode resonances are excited by the the tide, for  $\bar{\omega}/\Omega_s = (\pm\sqrt{105} - 7)/28$ . For  $\Omega_s = 0.1$  these roots correspond to  $\bar{\omega} = 0.012$  and  $\bar{\omega} = -0.062$ . For a core with a density and pressure gradient, like the one studied in this paper, inertial modes can be excited throughout the inertial range, but generally with an amplitude smaller than the response for the two above mentioned resonance frequencies.

Note that in Figs. 8 and 9, which show the  $t_0$  distributions obtained by the detailed numerical calculations for the more realistic stellar model considered here, two broad resonance dips are visible corresponding roughly with the above mentioned two resonant frequencies. In Fig. 10 we have plotted, for the positive resonance frequency  $\bar{\omega} = 0.0185$  ( $\Omega_s = 0.1$ ), the FL-coefficients of the radial and  $\theta$  displacement versus radial mesh number. It can be seen that the imaginary parts of the resonant inertial response in the core attain amplitudes large compared to those of the (high order) g-mode in the radiative envelope. Apparently the inertial mode in the core excites g-modes in the envelope to a level higher than normal, yielding the broad dip in the  $t_0$  curve.

At  $\bar{\omega} \simeq 0.007$  another strong resonance occurs with an inertial mode in the core. However, the resolution in the envelope is too poor to determine  $t_0$  for such low frequency response.

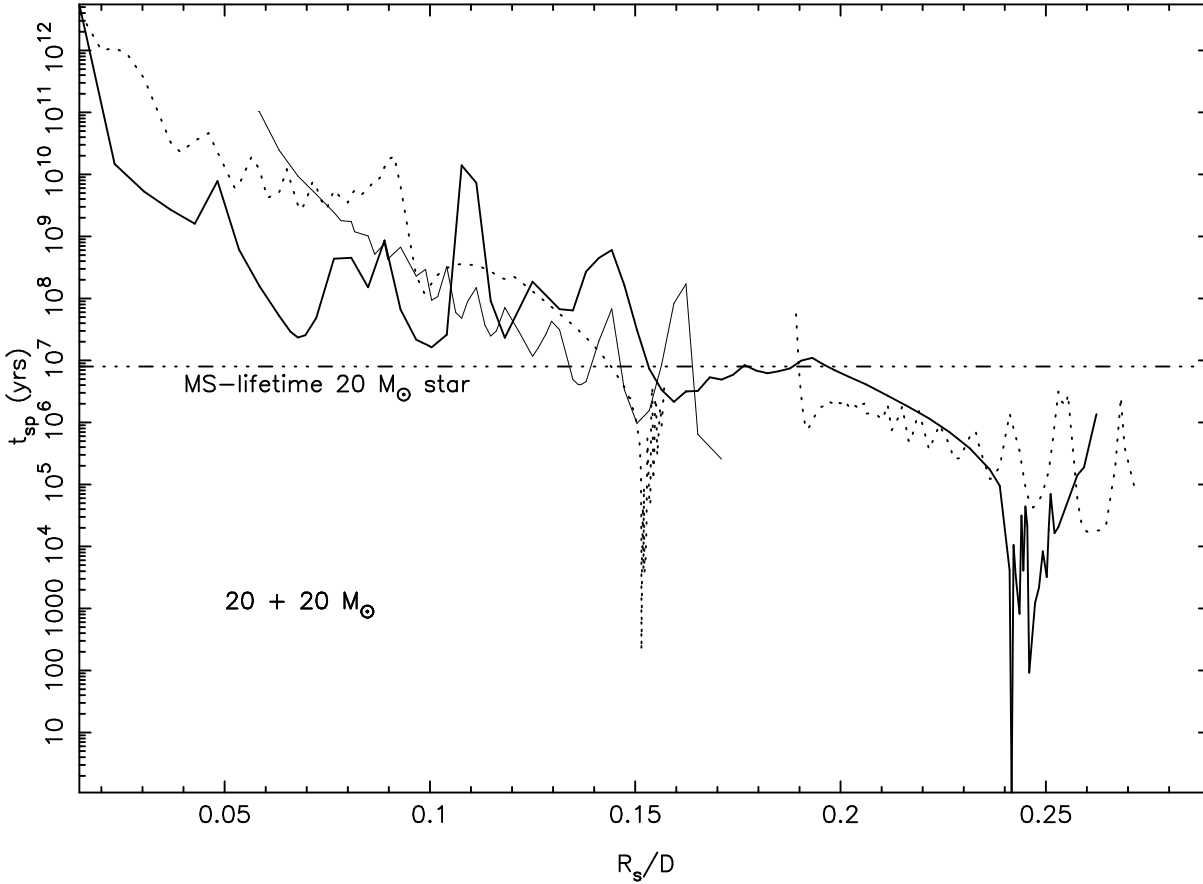


**Figure 11.** The tidal spin-up or spin-down timescale  $t_{sp}$  as a function of  $R_s/D$ , where  $D$  is the orbital separation, for a binary system consisting of two  $20 M_\odot$  unevolved stars. The full fat curve corresponds to a stellar spin rate  $\Omega_s = 0.2$ , the dotted curve to  $\Omega_s = 0.1$  and the thin full line to a non-rotating star. The spin up-time curve for  $\Omega_s = 0.2$  correspond to larger values of  $R_s/D$  than shown here.

#### 4.8 Comparison with observations

Giuricin, Mardirossian and Mezetti (1984 a,b,c) inspected a large sample of early type binaries and studied their orbital eccentricity and synchronism between orbital revolution and stellar spin rate. Their conclusion is that Zahn’s asymptotic expression (1977) for tidal effects can explain the majority of observed eccentricities. There remains, however, a not insignificant fraction of relatively wide early type binaries with nearly circular orbits that still require an explanation. Furthermore, these authors note a pronounced tendency towards synchronisation up to relative radii  $R_s/D \simeq 0.05$ , while Zahn’s asymptotic theory predicts a limiting separation for this corresponding to  $R_s/D \simeq 0.15$ .

To synchronise a wide (circular) system with equal masses and  $R_s/D = 0.05$  during the main sequence stage of duration  $\tau_{MS}$  of its early type components requires a time averaged ‘intrinsic’ spin-down time  $\langle t_0 \rangle \simeq (0.05)^6 \tau_{MS}$ , which for  $\tau_{MS} \simeq 8 \times 10^6$  year corresponds to  $\langle t_0 \rangle \simeq 0.1$  year.  $R_s/D = 0.10$  would require  $\langle t_0 \rangle \simeq 10$  years. That demands a strong tidal response, which is difficult to attain with radiative damping of dynamical tides, unless the tide is in continuous resonant interaction with a weakly damped mode. But note that in a wide binary with  $R_s/D = 0.05$  and mass ratio unity (which corresponds to  $P_b \simeq 30$  days) an early type star rotating with a period of 2.5 days ( $\Omega_s = 0.2$ ) encounters strong resonances with weakly damped, rotationally modified, retrograde g-modes for which  $t_0 \simeq 1$  year (Fig. 9). Hence it is expected to undergo significant spin down.

To visualize our numerical results we have plotted in Fig. 11 the spin-up or spin-down time as a function of  $R_s/D$  for a circular binary system consisting of two unevolved  $20M_\odot$  stars, by scaling the general results  $t_0(\bar{\omega})$  to this particular binary configuration, adopting  $\Omega_s = 0.2$  (full fat curve),  $\Omega_s = 0.1$  (dotted curve) and  $\Omega_s = 0$  (thin full line). The spin-up times for  $\Omega_s = 0.2$  are not shown, they correspond to  $R_s/D$  values larger than given in the figure.

It can be seen that with rotation the spin down time in wide binaries tend to be shorter, i.e. tidal effects can be significant even in binaries with  $R/D \simeq 0.06$ . It should be taken into account that the star is subject to internal (nuclear) evolution causing the core to shrink and the envelope to expand during the core hydrogen burning stage. The envelope expansion causes the star to spin down by about a factor 2 during the main sequence stage (this factor would be larger when the envelope decouples from the more rapidly spinning core). The core contraction, on the other hand, gives rise to increased gravity and

a shift of the g-mode frequencies to higher (absolute) values. Thus the internal evolution has significant effects on the tidal evolution of the binary (SP84). When a mode frequency shifts to higher frequency the radiative damping decreases and the corresponding  $t_0$  goes down, making it easier to synchronise the star.

What could further ease synchronisation is that the tides might induce differential rotation whereby the surface layers get synchronised and decoupled (to some extent) from the more rapidly spinning interior. Then apparent synchronisation of a main sequence star in quite wide binaries is relatively easy. Goldreich & Nicholson (1989) suggested that this is actually to be expected because the tidal despinning takes place where the g-modes are dissipated, i.e. initially in the surface layers of the star. When the surface layers have been synchronised, the gravity waves (excited near the core boundary) can no longer penetrate to the surface. When gravity waves approach the corotating surface layers their wavelength keeps diminishing until they are fully absorbed. The absorbed negative angular momentum carried by the gravity waves then leads to further spin down of the layers immediately beneath the corotating layers. Adopting this picture, the more rapidly spinning interior keeps its initial rotation rate with a slowly rotating, synchronized shell on top of it. Shear instabilities or other processes of angular momentum redistribution are expected to smooth this discontinuous angular velocity profile to some extent. Assuming that the  $t_0$  curve for the original uniform rotation rate remains approximately applicable, we deduce from Fig. 11 that for  $\Omega_s = 0.2$  the spin down time  $t_{sp}$  (required to reach corotation) is on average roughly 10 times longer than the star's main sequence lifetime for systems with  $0.15 \geq R/D \geq 0.06$ . Hereby we take into account that structural changes of the star due to stellar evolution shifts its modal spectrum, so that the star cannot remain stuck on a bump in the  $t_0$  curve. This would correspond to synchronisation of the outer several percent of the stellar mass, i.e. synchronisation down to a depth of  $r/R_s \simeq 0.6$  during the main sequence phase. It suggests that tides in rotating stars may cause 'apparent' synchronisation in quite wide binary systems.

## 5 DISCUSSION

We have studied the fully non-adiabatic tidal response of a slowly and uniformly rotating  $20 M_\odot$  ZAMS star to an  $l = m = 2$  perturbing potential in the low frequency, inertial regime. We solved the partial differential equations governing the response using a 2D-implicit finite difference scheme. In the work described here, the Coriolis force was included but the centrifugal force was neglected. This enabled us to work with spherically symmetric equilibrium models.

Our results show that, as expected, rotational effects can significantly influence the tidal response. We have extended the study of tidal effects to super-synchronous stars in which retrograde r-modes and rotationally modified retrograde g-modes are excited. The r-modes give rise to efficient spin-down in slightly super-synchronous stars, while the retrograde g-modes can give efficient despinning of highly super-synchronous early type stars in wide binaries. For all frequencies in the inertial regime inertial waves are excited in the core and convective surface shells. Consistent with analytic results derived for a simplified model with a constant density core (Papaloizou and Savonije 1997) the detailed numerical results show the existence of frequency intervals for which the tidal response is significantly enhanced due to resonance with an inertial mode in the core. The calculated broad resonance features indicate that the resonant inertial mode in the (almost adiabatic) core is damped by exciting gravity modes in the envelope to a level higher than normal. Assuming that the tides induce differential rotation by synchronising the outer parts of the early type star, while leaving its interior roughly unaltered, synchronisation may be achieved in a substantial part of the envelope during the main sequence phase, even in quite wide binary systems. This could explain the observed approximate synchronous rotation in some wide binary systems with  $R/D \simeq 0.05$ .

### Acknowledgment

This work was sponsored by the Stichting Nationale Computerfaciliteiten (National Computing Facilities Foundation, NCF) for the use of supercomputing facilities, with financial support from the Netherlands Organization for Scientific Research (NWO). We thank Marnix Witte for his help with the implementation of the opacity tables. JCP thanks the Anton Pannekoek Institute, and GJS is grateful to QMW for hospitality.

## REFERENCES

- Berthomieu G., Gonczy G., Graff Ph., Provost J., Rocca A., 1978, A&A, 70, 597.
- Cowling, T.G., 1941, MNRAS, 101, 367.
- Eckart, C., 1960, *Hydrodynamics of Oceans and Atmospheres*, Pergamon Press, Oxford.
- Eggleton P.P., 1972, MNRAS, 156, 361.
- Goldreich P., Nicholson Ph.D., 1989, ApJ, 342, 1079.
- Giuricin G., Mardirossian F., Mezzetti M., 1984a, A&A, 131, 152.
- Giuricin G., Mardirossian F., Mezzetti M., 1984a, A&A, 134, 365.
- Giuricin G., Mardirossian F., Mezzetti M., 1984b, A&A, 135, 393.
- Iglesias C.A., Rogers F.J., 1993, ApJ, 412, 752.

- Ledoux P., Walraven T., 1958. *Handbuch der Physik*, 51, 353.  
Lee U., Saio H., 1987, MNRAS, 224, 513.  
Lee U., Saio H., 1989, MNRAS, 237, 875.  
Provost J., Berthomieu C., Rocca A., 1981, A&A, 94, 126  
Papaloizou J.C.B., Pringle J.E., 1978, MNRAS, 182, 423.  
Papaloizou J.C.B., Savonije G.J. 1985, MNRAS, 213, 85.  
Papaloizou J.C.B., Savonije G.J. 1997, astro-ph/9706186.  
Pedlosky J. 1979, *Geophysical Fluid Dynamics*, (Berlin: Springer Verlag).  
Pols O.R., Tout C.A., Eggleton P.P. and Han Z., MNRAS, 274, 964.  
Rocca A., 1982, A&A, 111, 25.  
Saio H., 1982, ApJ, 256, 717.  
Savonije G.J., Papaloizou J.C.B., 1983, MNRAS, 203, 581.  
Savonije G.J., Papaloizou J.C.B., 1984, MNRAS, 207, 685.  
Savonije G.J., Papaloizou J.C.B. & Alberts, F., 1995, MNRAS, 277, 471 .  
Zahn J.P., 1977, A&A, 57, 383.



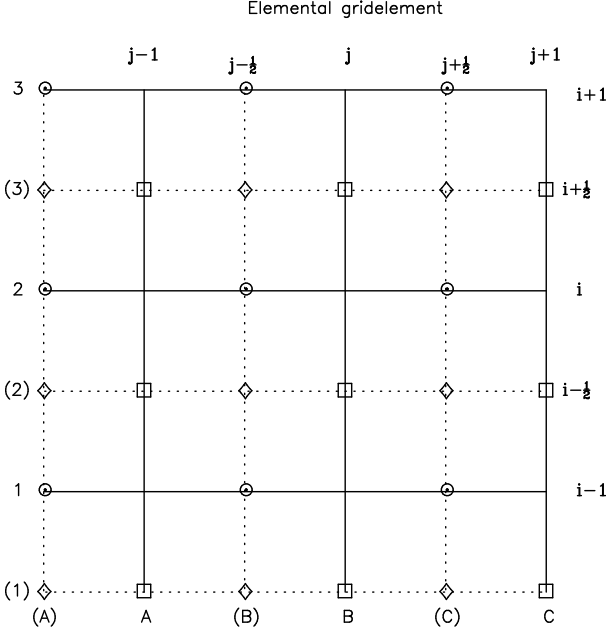


**Figure A1.** Schematic picture of the elemental gridcell for the three-level finite difference scheme used. The lines  $j = \text{constant}$  all intersect at the stellar centre. The symbols  $\odot$ ,  $\square$  and  $\diamond$  denote the location where the different variables are defined and the locus where the 7 difference equations are centred.

$\odot$  corresponds to  $\xi_r$  and  $F'_r$ ; centre of equations (A1,A6)

$\square$  corresponds to  $\xi_\theta$  and  $F'_\theta$ ; centre of equations (A2,A7)

$\diamond$  corresponds to  $\xi_\varphi$ ,  $\rho'$  and  $T'$ ; centre of equations (A3,A4 and A5)

## APPENDIX A: THE FINITE DIFFERENCE EQUATIONS (FDE'S)

We solve, as function of  $r$  and  $\theta$ , the set (6)–(12) of seven linearized partial differential equations, together with boundary conditions, for the seven complex quantities  $\xi_r$ ,  $\xi_\theta$ ,  $\xi_\varphi$ ,  $\left(\frac{\rho'}{\rho}\right)$ ,  $\left(\frac{T'}{T}\right)$ ,  $\left(\frac{F'_r}{F}\right)$  and  $\left(\frac{F'_\theta}{F}\right)$  by rewriting them as a set of finite difference equations on a polar  $(r, \theta)$  grid in a meridional plane of the star. Because the forcing has symmetry about the equatorial plane ( $\theta = \pi/2$ ) we need only consider the first quadrant:  $0 \leq \theta \leq \pi/2$ . The index  $i = 1, N_r$  runs along radius (from  $r = 0$  to  $r = R_s$ ) and the index  $j = 1, N_\theta$  runs in the  $\theta$ -direction (from  $\theta = 0$  to  $\theta = \pi/2$ ).

Note that for stable numerical results care is needed to construct the FDE's. The set of FDE's given below yielded satisfactory numerical results. These FDE's approximate the PDE's in such a way that for  $\Omega_s \rightarrow 0$  they too become separable in  $r$  and  $\theta$ . For numerical stability we use a staggered mesh, so that the various perturbed quantities to be solved for are not all defined at the same location. See Fig. A1 for a schematic picture of an elemental gridcell for the three-level difference scheme used in the calculations.

The adopted radial grid is not equidistant. The  $\theta$ -grid is for  $\theta > \frac{\pi}{4}$  equidistant in  $\mu = \cos \theta$  with  $\Delta\mu = \mu_j - \mu_{j-1}$  while it is for  $\theta \leq \frac{\pi}{4}$  equidistant ( $\Delta\nu = \nu_j - \nu_{j-1}$ ) in  $\nu = \sin \theta$ . With this  $\theta$ -grid we have for  $N_\theta = 64$  adequate resolution, especially both near the rotation axis and near the stellar equator. At the transition point  $j = N_h$  (corresponding to  $\theta = \frac{\pi}{4}$ )  $\nu = \mu$ . However, because of the staggered mesh, for  $2^{nd}$  order derivatives expressions for a non-equidistant ( $\theta$ -)grid should be taken at that point.

The radial equation of motion (6) is approximated by

$$\begin{aligned}
 & \left[ \bar{\sigma}^2 \rho_i R_s \right] \left( \frac{\xi_r}{R_s} \right)_{i,j-\frac{1}{2}} + \left[ i \bar{\sigma} \Omega_s \nu_{j-\frac{1}{2}} \rho_i R_s \right] \left( \frac{\xi_\varphi}{R_s} \right)_{i-\frac{1}{2},j-\frac{1}{2}} + \left[ i \bar{\sigma} \Omega_s \nu_{j-\frac{1}{2}} \rho_i R_s \right] \left( \frac{\xi_\varphi}{R_s} \right)_{i+\frac{1}{2},j-\frac{1}{2}} \\
 & + \left[ \frac{P_{X\rho} \rho_{i-\frac{1}{2}}}{(r_{i+\frac{1}{2}} - r_{i-\frac{1}{2}})} + \frac{1}{2} \frac{P_{i+\frac{1}{2}} - P_{i-\frac{1}{2}}}{(r_{i+\frac{1}{2}} - r_{i-\frac{1}{2}})} \right] \left( \frac{\rho'}{\rho} \right)_{i-\frac{1}{2},j-\frac{1}{2}} - \left[ \frac{P_{X\rho} \rho_{i+\frac{1}{2}}}{(r_{i+\frac{1}{2}} - r_{i-\frac{1}{2}})} - \frac{1}{2} \frac{P_{i+\frac{1}{2}} - P_{i-\frac{1}{2}}}{(r_{i+\frac{1}{2}} - r_{i-\frac{1}{2}})} \right] \left( \frac{\rho'}{\rho} \right)_{i+\frac{1}{2},j-\frac{1}{2}} \\
 & + \left[ \frac{P_{XT} T_{i-\frac{1}{2}}}{(r_{i+\frac{1}{2}} - r_{i-\frac{1}{2}})} \right] \left( \frac{T'}{T} \right)_{i-\frac{1}{2},j-\frac{1}{2}} - \left[ \frac{P_{XT} T_{i+\frac{1}{2}}}{(r_{i+\frac{1}{2}} - r_{i-\frac{1}{2}})} \right] \left( \frac{T'}{T} \right)_{i+\frac{1}{2},j-\frac{1}{2}} = 6f\rho_i r_i \nu_{j-\frac{1}{2}}^2
 \end{aligned} \tag{A1}$$

The  $\theta$ -equation of motion (7) is approximated by

$$\left[ \bar{\sigma}^2 \rho_{i-\frac{1}{2}} R_s \right] \left( \frac{\xi_\theta}{R_s} \right)_{i-\frac{1}{2},j} + i \bar{\sigma} \Omega_s \rho_{i-\frac{1}{2}} R_s \left[ \mu_{j+\frac{1}{2}} \left( \frac{\xi_\varphi}{R_s} \right)_{i-\frac{1}{2},j+\frac{1}{2}} + \mu_{j-\frac{1}{2}} \left( \frac{\xi_\varphi}{R_s} \right)_{i-\frac{1}{2},j-\frac{1}{2}} \right]$$

$$-\left(\frac{P\chi\rho}{r}\right)_{i-\frac{1}{2}} \Delta \left[ \left(\frac{\rho'}{\rho}\right)_{i-\frac{1}{2},j+\frac{1}{2}} - \left(\frac{\rho'}{\rho}\right)_{i-\frac{1}{2},j-\frac{1}{2}} \right] - \left(\frac{P\chi T}{r}\right)_{i-\frac{1}{2}} \Delta \left[ \left(\frac{T'}{T}\right)_{i-\frac{1}{2},j+\frac{1}{2}} - \left(\frac{T'}{T}\right)_{i-\frac{1}{2},j-\frac{1}{2}} \right] = 6f\rho_{i-\frac{1}{2}} r_{i-\frac{1}{2}} \nu_j \mu_j \quad (\text{A2})$$

where  $\Delta = \frac{\mu_j}{\Delta\nu}$  for  $j \leq N_h$  and  $\Delta = \frac{-\nu_j}{\Delta\mu}$  for  $j > N_h$ .

The  $\varphi$ -equation of motion (8) becomes

$$\begin{aligned} -i\bar{\sigma}\Omega_s \rho_{i-\frac{1}{2}} R_s \nu_{j-\frac{1}{2}} \left[ \left(\frac{\xi_r}{R_s}\right)_{i-1,j-\frac{1}{2}} + \left(\frac{\xi_r}{R_s}\right)_{i,j-\frac{1}{2}} \right] - i\bar{\sigma}\Omega_s \rho_{i-\frac{1}{2}} R_s \mu_{j-\frac{1}{2}} \left[ \left(\frac{\xi_\theta}{R_s}\right)_{i-\frac{1}{2},j-1} + \left(\frac{\xi_\theta}{R_s}\right)_{i-\frac{1}{2},j} \right] + \bar{\sigma}^2 \rho_{i-\frac{1}{2}} R_s \left(\frac{\xi_\varphi}{R_s}\right)_{i-\frac{1}{2},j-\frac{1}{2}} \\ + \left[ \frac{im}{\nu_{j-\frac{1}{2}}} \left(\frac{P\chi\rho}{r}\right)_{i-\frac{1}{2}} \right] \left(\frac{\rho'}{\rho}\right)_{i-\frac{1}{2},j-\frac{1}{2}} + \left[ \frac{im}{\nu_{j-\frac{1}{2}}} \left(\frac{P\chi T}{r}\right)_{i-\frac{1}{2}} \right] \left(\frac{T'}{T}\right)_{i-\frac{1}{2},j-\frac{1}{2}} = -3imf r_{i-\frac{1}{2}} \rho_{i-\frac{1}{2}} \nu_{j-\frac{1}{2}} \end{aligned} \quad (\text{A3})$$

The equation of continuity (9) becomes

$$\begin{aligned} \left[ \frac{\rho_i r_i^2 R_s}{\rho_{i-\frac{1}{2}} r_{i-\frac{1}{2}}^2 (r_i - r_{i-1})} \right] \left(\frac{\xi_r}{R_s}\right)_{i,j-\frac{1}{2}} - \left[ \frac{\rho_{i-1} r_{i-1}^2 R_s}{\rho_{i-\frac{1}{2}} r_{i-\frac{1}{2}}^2 (r_i - r_{i-1})} \right] \left(\frac{\xi_r}{R_s}\right)_{i-1,j-\frac{1}{2}} \\ + T_1 \left(\frac{\xi_\theta}{R_s}\right)_{i-\frac{1}{2},j-1} + T_2 \left(\frac{\xi_\theta}{R_s}\right)_{i-\frac{1}{2},j} - \left[ \frac{im R_s}{r_{i-\frac{1}{2}} \nu_{j-\frac{1}{2}}} \right] \left(\frac{\xi_\varphi}{R_s}\right)_{i-\frac{1}{2},j-\frac{1}{2}} + \left(\frac{\rho'}{\rho}\right)_{i-\frac{1}{2},j-\frac{1}{2}} = 0 \end{aligned} \quad (\text{A4})$$

where for  $j \leq N_h$  the terms  $T_1$  and  $T_2$  are defined as

$$T_1 = \left[ \frac{(1-2\nu_{j-\frac{1}{2}}^2) R_s}{2r_{i-\frac{1}{2}} \nu_{j-\frac{1}{2}} \mu_{j-\frac{1}{2}}} - \frac{\mu_{j-\frac{1}{2}}^2 R_s}{\mu_{j-1} r_{i-\frac{1}{2}} \Delta\nu} \right] \text{ and } T_2 = \left[ \frac{(1-2\nu_{j-\frac{1}{2}}^2) R_s}{2r_{i-\frac{1}{2}} \nu_{j-\frac{1}{2}} \mu_{j-\frac{1}{2}}} + \frac{\mu_{j-\frac{1}{2}}^2 R_s}{\mu_j r_{i-\frac{1}{2}} \Delta\nu} \right]$$

For  $j > N_h$  these terms are given by

$$T_1 = \left[ \frac{\mu_{j-\frac{1}{2}}}{r_{i-\frac{1}{2}} \nu_{j-\frac{1}{2}}} R_s + \frac{\nu_{j-\frac{1}{2}}^2}{\nu_{j-1} r_{i-\frac{1}{2}} \Delta\mu} R_s \right] \text{ and } T_2 = \left[ \frac{\mu_{j-\frac{1}{2}}}{r_{i-\frac{1}{2}} \nu_{j-\frac{1}{2}}} R_s - \frac{\nu_{j-\frac{1}{2}}^2}{\nu_j r_{i-\frac{1}{2}} \Delta\mu} R_s \right]$$

The energy equation (10) is approximated by

$$\begin{aligned} \left[ \frac{\left(\frac{P_i - P_{i-1}}{P_{i-\frac{1}{2}}}\right)}{(r_i - r_{i-1})} - \Gamma_{1i-\frac{1}{2}} \frac{\left(\frac{\rho_i - \rho_{i-1}}{\rho_{i-\frac{1}{2}}}\right)}{(r_i - r_{i-1})} \right] \frac{R_s}{2} \left(\frac{\xi_r}{R_s}\right)_{i,j-\frac{1}{2}} + \left[ \frac{\left(\frac{P_i - P_{i-1}}{P_{i-\frac{1}{2}}}\right)}{(r_i - r_{i-1})} - \Gamma_{1i-\frac{1}{2}} \frac{\left(\frac{\rho_i - \rho_{i-1}}{\rho_{i-\frac{1}{2}}}\right)}{(r_i - r_{i-1})} \right] \frac{R_s}{2} \left(\frac{\xi_r}{R_s}\right)_{i-1,j-\frac{1}{2}} \\ + \left[ -\frac{i\eta_{i-\frac{1}{2}}}{(r_i - r_{i-1})} \left( \frac{r_i^2}{r_{i-\frac{1}{2}}^2} + \frac{(F_i - F_{i-1})}{2F_{i-\frac{1}{2}}} \right) \right] \left(\frac{F'_r}{F}\right)_{i,j-\frac{1}{2}} + \left[ -\frac{i\eta_{i-\frac{1}{2}}}{(r_i - r_{i-1})} \left( -\frac{r_{i-1}^2}{r_{i-\frac{1}{2}}^2} + \frac{(F_i - F_{i-1})}{2F_{i-\frac{1}{2}}} \right) \right] \left(\frac{F'_r}{F}\right)_{i-1,j-\frac{1}{2}} \\ + T_1 \left(\frac{F'_\theta}{F}\right)_{i-\frac{1}{2},j} + T_2 \left(\frac{F'_\theta}{F}\right)_{i-\frac{1}{2},j-1} + \left[ \chi_T + \left(\frac{m}{r_{i-\frac{1}{2}} \nu_{j-\frac{1}{2}}}\right)^2 \frac{i\eta_{i-\frac{1}{2}}}{\left(\frac{T_i - T_{i-1}}{T_{i-\frac{1}{2}}}\right)} + \left(\frac{T'}{T}\right)_{i-\frac{1}{2},j-\frac{1}{2}} \right] = [\Gamma_1 - \chi_\rho]_{i-\frac{1}{2}} \left(\frac{\rho'}{\rho}\right)_{i-\frac{1}{2},j-\frac{1}{2}} \end{aligned} \quad (\text{A5})$$

where for  $j \leq N_h$

$$T_1 = -\frac{i\eta_{i-\frac{1}{2}}}{r_{i-\frac{1}{2}} \mu_j} \left[ \mu_{j-\frac{1}{2}}^2 \left( \frac{1}{\Delta\nu} + \frac{1}{2\nu_{j-\frac{1}{2}}} - \frac{1}{2}\nu_{j-\frac{1}{2}} \right) \right] \text{ and } T_2 = -\frac{i\eta_{i-\frac{1}{2}}}{r_{i-\frac{1}{2}} \mu_{j-1}} \left[ \mu_{j-\frac{1}{2}}^2 \left( \frac{-1}{\Delta\nu} + \frac{1}{2\nu_{j-\frac{1}{2}}} - \frac{1}{2}\nu_{j-\frac{1}{2}} \right) \right]$$

whereas for  $j > N_h$  these terms are:

$$T_1 = -\frac{i\eta_{i-\frac{1}{2}}}{r_{i-\frac{1}{2}} \nu_j} \left[ \mu_{j-\frac{1}{2}} - \frac{\nu_{j-\frac{1}{2}}^2}{\Delta\mu} \right] \text{ and } T_2 = -\frac{i\eta_{i-\frac{1}{2}}}{r_{i-\frac{1}{2}} \nu_{j-1}} \left[ \mu_{j-\frac{1}{2}} + \frac{\nu_{j-\frac{1}{2}}^2}{\Delta\mu} \right]$$

The radial energy diffusion equation (11) is approximated by

$$\begin{aligned} \left(\frac{F'_r}{F}\right)_{i,j-\frac{1}{2}} + \frac{1}{2} ((\kappa_\rho)_i + 1) \left[ \left(\frac{\rho'}{\rho}\right)_{i-\frac{1}{2},j-\frac{1}{2}} + \left(\frac{\rho'}{\rho}\right)_{i+\frac{1}{2},j-\frac{1}{2}} \right] + \left[ \frac{1}{2} (\kappa_T)_i - 2 - \frac{T_i}{T_{i+\frac{1}{2}} - T_{i-\frac{1}{2}}} \right] \left(\frac{T'}{T}\right)_{i+\frac{1}{2},j-\frac{1}{2}} \\ + \left[ \frac{1}{2} (\kappa_T)_i - 2 + \frac{T_i}{T_{i+\frac{1}{2}} - T_{i-\frac{1}{2}}} \right] \left(\frac{T'}{T}\right)_{i-\frac{1}{2},j-\frac{1}{2}} = 0 \end{aligned} \quad (\text{A6})$$

Finally, the energy diffusion in the  $\theta$ -direction (12) is approximated by

$$\frac{r_i - r_{i-1}}{T_i - T_{i-1}} \frac{T_{i-\frac{1}{2}}}{r_{i-\frac{1}{2}}} \Delta \left[ \left(\frac{T'}{T}\right)_{i-\frac{1}{2},j-\frac{1}{2}} - \left(\frac{T'}{T}\right)_{i-\frac{1}{2},j+\frac{1}{2}} \right] + \left(\frac{F'_\theta}{F}\right)_{i-\frac{1}{2},j} = 0 \quad (\text{A7})$$

where  $\Delta$  was defined in equation (A2).

### A1 The viscous terms

The viscous terms (16-17) added to the equations of motion contain second order derivatives and must therefore be defined on three levels of the grid. Again the finite differences are constructed in such a way that the expressions retain separability in  $r$  and  $\theta$ . To that end the derivatives with respect to  $\mu$  in equations (16-17) are for  $j \leq N_h$  expressed as

$$\frac{\partial \xi_r}{\partial \mu} = -\frac{\mu}{\nu} \bar{\xi}_r - \frac{\partial \bar{\xi}_r}{\partial \nu}$$

and

$$\frac{\partial^2}{\partial \mu^2} \xi_r = -\frac{\bar{\xi}_r}{\nu^3} + \frac{1-2\nu^2}{\nu^2} \frac{\partial \bar{\xi}_r}{\partial \nu} + \frac{\mu^2}{\nu} \frac{\partial^2}{\partial \nu^2} \bar{\xi}_r$$

where for  $\Omega_s = 0$  we have  $\bar{\xi}_r \equiv \frac{\xi_r}{\nu} \propto \nu$ . For  $\xi_\theta$  the  $\mu$ -derivatives are expressed as

$$\frac{\partial^2}{\partial \mu^2} \xi_\theta = -\left(3\frac{\mu}{\nu} + \frac{\mu^3}{\nu^3}\right) \frac{d\bar{\xi}_\theta}{d\nu} + \frac{\mu^3}{\nu^2} \frac{\partial^2}{\partial \nu^2} \bar{\xi}_\theta$$

where for  $\Omega_s = 0$  we have  $\bar{\xi}_\theta \equiv \frac{\xi_\theta}{\mu} \propto \nu$ . With  $\alpha_i = i\bar{\sigma}R_s(\zeta/r^2)_i$ , the radial derivatives to be added to the equation of radial motion (A1) become

$$\begin{aligned} & -\frac{\alpha_i}{\Delta_3} \left[ \frac{(\rho\zeta r^2)_{i+\frac{1}{2}} - (\rho\zeta r^2)_{i-\frac{1}{2}}}{\zeta_i(r_{i+\frac{1}{2}} - r_{i-\frac{1}{2}})} \frac{\Delta_1}{\Delta_2} - \frac{2(\rho r^2)_i}{\Delta_2} \right] \left( \frac{\xi_r}{R_s} \right)_{i-1, j-\frac{1}{2}} + \frac{\alpha_i}{\Delta_3} \left[ \frac{(\rho\zeta r^2)_{i+\frac{1}{2}} - (\rho\zeta r^2)_{i-\frac{1}{2}}}{\zeta_i(r_{i+\frac{1}{2}} - r_{i-\frac{1}{2}})} \left( \frac{\Delta_1}{\Delta_2} - \frac{\Delta_2}{\Delta_1} \right) \right] \left( \frac{\xi_r}{R_s} \right)_{i, j-\frac{1}{2}} \\ & - \frac{\alpha_i}{\Delta_3} \left[ 2(\rho r^2)_i \left( \frac{1}{\Delta_1} + \frac{1}{\Delta_2} \right) \right] \left( \frac{\xi_r}{R_s} \right)_{i, j-\frac{1}{2}} + \frac{\alpha_i}{\Delta_3} \left[ \frac{(\rho\zeta r^2)_{i+\frac{1}{2}} - (\rho\zeta r^2)_{i-\frac{1}{2}}}{\zeta_i(r_{i+\frac{1}{2}} - r_{i-\frac{1}{2}})} \frac{\Delta_2}{\Delta_1} + \frac{2(\rho r^2)_i}{\Delta_1} \right] \left( \frac{\xi_r}{R_s} \right)_{i+1, j-\frac{1}{2}} \end{aligned} \quad (\text{A8})$$

where  $\Delta_1 = r_{i+1} - r_i$ ,  $\Delta_2 = r_i - r_{i-1}$  and  $\Delta_3 = r_{i+1} - r_{i-1}$ .

The  $\theta$ -derivatives to be added to the equation of radial motion become for  $j \leq N_h$

$$\begin{aligned} & \frac{\alpha_i \rho_i}{\Delta_3} \left[ -\frac{3-4\nu_{j-\frac{1}{2}}^2}{\nu_{j-\frac{3}{2}}} \frac{\Delta_1}{\Delta_2} + \frac{2\mu_{j-\frac{1}{2}}^2 \nu_{j-\frac{1}{2}}}{\nu_{j-\frac{3}{2}} \Delta_2} \right] \xi_{i, j-\frac{3}{2}} - \frac{\alpha_i \rho_i}{\Delta_3} \left[ 2 + \frac{3}{\nu_{j-\frac{1}{2}}^2} + 2\mu_{j-\frac{1}{2}}^2 \left( \frac{1}{\Delta_1} + \frac{1}{\Delta_2} \right) \right] \left( \frac{\xi_r}{R_s} \right)_{i, j-\frac{1}{2}} \\ & - \frac{\alpha_i \rho_i}{\Delta_3} \left[ \frac{3-4\nu_{j-\frac{1}{2}}^2}{\nu_{j-\frac{1}{2}}} \left( \frac{\Delta_2}{\Delta_1} - \frac{\Delta_1}{\Delta_2} \right) \right] \left( \frac{\xi_r}{R_s} \right)_{i, j-\frac{1}{2}} + \frac{\alpha_i \rho_i}{\Delta_3} \left[ \frac{3-4\nu_{j-\frac{1}{2}}^2}{\nu_{j+\frac{1}{2}}} \frac{\Delta_2}{\Delta_1} + \frac{2\mu_{j-\frac{1}{2}}^2 \nu_{j-\frac{1}{2}}}{\nu_{j+\frac{1}{2}} \Delta_1} \right] \left( \frac{\xi_r}{R_s} \right)_{i, j+\frac{1}{2}} \end{aligned} \quad (\text{A9})$$

where  $\Delta_1 = \nu_{j+\frac{1}{2}} - \nu_{j-\frac{1}{2}}$ ,  $\Delta_2 = \nu_{j-\frac{1}{2}} - \nu_{j-\frac{3}{2}}$  and  $\Delta_3 = \nu_{j+\frac{1}{2}} - \nu_{j-\frac{3}{2}}$ . Note that at the transition point  $j = N_h$  the grid is not equidistant (neither in  $\mu$  nor  $\nu$ ) and that it is essential to use the expressions for non-equidistant mesh given here. For  $j > N_h$  these derivatives become

$$\begin{aligned} & \frac{\alpha_i \rho_i}{\Delta_3} \left[ \frac{2\nu_{j-\frac{1}{2}}^2}{\Delta_2} + 2\mu_{j-\frac{1}{2}} \frac{\Delta_1}{\Delta_2} \right] \left( \frac{\xi_r}{R_s} \right)_{i, j-\frac{3}{2}} - \frac{\alpha_i \rho_i}{\Delta_3} \left[ 2\nu_{j-\frac{1}{2}}^2 \left( \frac{1}{\Delta_1} + \frac{1}{\Delta_2} \right) + \frac{4}{\nu_{j-\frac{1}{2}}^2} \right] \left( \frac{\xi_r}{R_s} \right)_{i, j-\frac{1}{2}} \\ & + \frac{\alpha_i \rho_i}{\Delta_3} \left[ 2\mu_{j-\frac{1}{2}} \left( \frac{\Delta_2}{\Delta_1} - \frac{\Delta_1}{\Delta_2} \right) \right] \left( \frac{\xi_r}{R_s} \right)_{i, j-\frac{1}{2}} + \frac{\alpha_i \rho_i}{\Delta_3} \left[ \frac{2\nu_{j-\frac{1}{2}}^2}{\Delta_1} - 2\mu_{j-\frac{1}{2}} \frac{\Delta_2}{\Delta_1} \right] \left( \frac{\xi_r}{R_s} \right)_{i, j+\frac{1}{2}} \end{aligned} \quad (\text{A10})$$

where now  $\Delta_1 = \mu_{j+\frac{1}{2}} - \mu_{j-\frac{1}{2}}$ ,  $\Delta_2 = \mu_{j-\frac{1}{2}} - \mu_{j-\frac{3}{2}}$  and  $\Delta_3 = \mu_{j+\frac{1}{2}} - \mu_{j-\frac{3}{2}}$  and similarly for the  $\theta$ -equation of motion.

### APPENDIX B: NUMERICAL SOLUTION TECHNIQUE

Let us introduce the following definition for the perturbation vector  $\mathbf{X}_{i,j}$  at each gridpoint centre  $(i, j)$ , consistent with Fig. A1

$$\mathbf{X}_{i,j} = \left( \left[ \frac{\xi_r}{R_s} \right]_{i, j-\frac{1}{2}}, \left[ \frac{F'_r}{F} \right]_{i, j-\frac{1}{2}}, \left[ \frac{\xi_\theta}{R_s} \right]_{i-\frac{1}{2}, j}, \left[ \frac{F'_\theta}{F} \right]_{i-\frac{1}{2}, j}, \left[ \frac{\xi_\varphi}{R_s} \right]_{i-\frac{1}{2}, j-\frac{1}{2}}, \left[ \frac{\rho'}{\rho} \right]_{i-\frac{1}{2}, j-\frac{1}{2}}, \left[ \frac{T'}{T} \right]_{i-\frac{1}{2}, j-\frac{1}{2}} \right)^t \quad (\text{B1})$$

where  $F$ ,  $\rho$  and  $T$  respectively denote the local unperturbed energy-flux, density and temperature and  $R_s$  the stellar radius.

Then the finite difference equations (A1-A7) corresponding to the 7 linearized partial differential equations (6)–(12) extended with the viscous terms can for each step  $(i, j)$  be expressed as a single matrix equation

$$A_1 \mathbf{X}_{i-1, j-1} + B_1 \mathbf{X}_{i-1, j} + C_1 \mathbf{X}_{i-1, j+1} + A_2 \mathbf{X}_{i, j-1} + B_2 \mathbf{X}_{i, j} + C_2 \mathbf{X}_{i, j+1} + A_3 \mathbf{X}_{i+1, j-1} + B_3 \mathbf{X}_{i+1, j} + C_3 \mathbf{X}_{i+1, j+1} + D = 0 \quad (\text{B2})$$

where the  $7 \times 7$ -matrices  $A_l$ ,  $B_l$  and  $C_l$ , for  $l = 1, 2, 3$  are complex and defined in terms of the unperturbed stellar model.

The elimination procedure that solves for the perturbation vectors  $\mathbf{X}_{i,j}$  is initiated by applying the boundary conditions at the stellar centre ( $i - 1 = 0$ ), where we require  $\xi_r$  and  $F'_r$  to vanish. The remaining five components of the perturbation vector  $\mathbf{X}_{0,j}$  are located outside the grid, see Fig. (A1), and need not be defined. Hence, for  $i = 1$  the terms with the coefficient matrices  $A_1$ ,  $B_1$  and  $C_1$  disappear from the finite difference equation (FDE) (B2) for all  $j$ .

By applying the boundary conditions at the stellar rotation axis ( $j - 1 = 0$ ) and requiring  $\xi_\theta$  and  $F'_\theta$  to vanish, and noting that the remaining five components of the perturbation vectors  $\mathbf{X}_{i,0}$  need not be defined (see Fig. A1), we conclude that for  $j = 1$  the terms with the coefficient matrices  $A_l$ , with  $l = 1, 2, 3$ , also disappear from the FDE (B2) for all  $i$ .

For  $i = 1$ ,  $j = 1$  the simplified FDE's can thus be written as

$$B_2 \mathbf{X}_{1,1} + C_2 \mathbf{X}_{1,2} + B_3 \mathbf{X}_{2,1} + C_3 \mathbf{X}_{2,2} + D = 0 \quad (\text{B3})$$

By inverting matrix  $B_2$  we immediately find the relation:

$$\mathbf{X}_{1,1} = -B_2^{-1} C_2 \mathbf{X}_{1,2} - B_2^{-1} B_3 \mathbf{X}_{2,1} - B_2^{-1} C_3 \mathbf{X}_{2,2} - B_2^{-1} D \quad (\text{B4})$$

The elimination procedure is continued by stepping up  $j$  for given  $i = 1$ . For  $j = 2$  the vector  $\mathbf{X}_{1,j-1}$  no longer vanishes, but it can be eliminated by substituting relation (B4) for  $\mathbf{X}_{1,j-1}$  into the FDE. After again multiplying by the inverted matrix  $B_2^{-1}$  we obtain a relation of the form

$$\mathbf{X}_{1,j} = \alpha^{1,j} \mathbf{X}_{1,j+1} + \sum_{l=1}^{j+1} \beta_l^{1,j} \mathbf{X}_{2,l} + \gamma^{1,j} \quad (\text{B5})$$

where  $\alpha^{1,j}$ ,  $\beta_l^{1,j}$  are complex  $7 \times 7$ -matrices and  $\gamma^{1,j}$  is a 7-vector.

For  $j > 2$  expression (B5) is applied after every step  $j$  to eliminate  $\mathbf{X}_{1,j}$  from all previous steps ( $j - 1, j - 2, \dots, 1$ ). After repeating the elimination procedure until  $j = N_\theta$  we can apply the equatorial symmetry conditions

$$\mathbf{X}_{1,N_\theta+1} = \mathcal{S} \mathbf{X}_{1,N_\theta} \quad (\text{B6})$$

where  $\mathcal{S}$  is a diagonal  $7 \times 7$ -matrix. Its diagonal elements corresponding to  $\xi_\theta$  and  $F'_\theta$  are  $-1$ , while all remaining diagonal elements are 1. Using these symmetry relations to eliminate  $\mathbf{X}_{1,N_\theta+1}$ , relation (B5) for  $\mathbf{X}_{1,N_\theta}$  can be re-expressed as

$$\mathbf{X}_{1,N_\theta} = \sum_{l=1}^{N_\theta} \beta_l^{1,N_\theta} \mathbf{X}_{2,l} + \gamma^{1,N_\theta} \quad (\text{B7})$$

where  $\beta_l^{1,N_\theta}$  and  $\gamma^{1,N_\theta}$  have been redefined.

After substituting the above expression for  $\mathbf{X}_{1,N_\theta}$  in all previously obtained results, we have eliminated all unknowns  $\mathbf{X}_{1,k}$  on the right hand side of expression (B5) and we end up with the set of relations (for  $k = 1, 2, 3, \dots, N_\theta$ )

$$\mathbf{X}_{1,k} = \sum_{l=1}^{N_\theta} \beta_l^{1,k} \mathbf{X}_{2,l} + \gamma^{1,k} \quad (\text{B8})$$

where the  $\beta_l^{1,k}$  and  $\gamma^{1,k}$  have been updated.

We can now step up  $i$  and start a new strike  $j = 1, 2, \dots, N_\theta$  (for  $i = 2, 3, \dots, N_r$ ). For  $i > 1$  the perturbation vectors  $\mathbf{X}_{i-1,k}$  no longer vanish in the FDE. However, relations (B8) obtained in the previous strike  $i - 1$  can now be used to eliminate these perturbation vectors from the FDE. To this end the latter relations must be updated after every elimination step ( $i, j$ ) to eliminate all  $\mathbf{X}_{i,l}$  with  $l < j$  from the summation on the right hand side of (B8). For step ( $i, j$ ) this results in an expression of the form (for  $k = j - 1, j, j + 1, \dots, N_\theta$ )

$$\mathbf{X}_{i-1,k} = \alpha^{i-1,k} \mathbf{X}_{i,j} + \sum_{l=1}^j \beta_l^{i-1,k} \mathbf{X}_{i+1,l} + \sum_{l=j+1}^{N_\theta} \beta_l^{i-1,k} \mathbf{X}_{i,l} + \gamma^{i-1,k} \quad (\text{B9})$$

From the previous elimination step ( $i, j - 1$ ) of the current strike  $i$  we have

$$\mathbf{X}_{i,j-1} = \alpha^{i,j-1} \mathbf{X}_{i,j} + \sum_{l=1}^j \beta_l^{i,j-1} \mathbf{X}_{i+1,l} + \sum_{l=j+1}^{N_\theta} \beta_l^{i,j-1} \mathbf{X}_{i,l} + \gamma^{i,j-1} \quad (\text{B10})$$

After substituting these results in the FDE (B2) for step ( $i, j$ ), all terms left of  $B_2 \mathbf{X}_{i,j} + \dots$  can be eliminated and the FDE is cast in the form

$$B_2 \mathbf{X}_{i,j} + C_2 \mathbf{X}_{i,j+1} + \sum_{l=1}^{j+1} \beta_l^{i,j} \mathbf{X}_{i+1,l} + \sum_{l=j+2}^{N_\theta} \beta_l^{i,j} \mathbf{X}_{i,l} + D = 0 \quad (\text{B11})$$

where  $B_2$ ,  $C_2$  and  $D$  have been redefined to collect the various coefficients of the corresponding vectors.

By again multiplying the FDE with the inverted matrix  $B_2^{-1}$  the vector  $\mathbf{X}_{i,j}$  can be expressed as

$$\mathbf{X}_{i,j} = \alpha^{i,j} \mathbf{X}_{i,j+1} + \sum_{l=1}^{j+1} \beta_l^{i,j} \mathbf{X}_{i+1,l} + \sum_{l=j+2}^{N_\theta} \beta_l^{i,j} \mathbf{X}_{i,l} + \gamma^{i,j} \quad (\text{B12})$$

which is of the same format as the result of the previous elimination step (B10). The current elimination step  $(i, j)$  is terminated by updating expressions (B9-B10). To this end expression (B12) for  $\mathbf{X}_{i,j}$  is substituted on their right hand sides. Equation (B9) must be updated for all  $k \geq j$ .

After repeating this elimination procedure until  $j = N_\theta$  the equatorial boundary conditions can be applied after which the stored relations for this strike  $i$  can be written as ( $k = 1, 2, \dots, N_\theta$ )

$$\mathbf{X}_{i,k} = \sum_{l=1}^{N_\theta} \beta_l^{i,k} \mathbf{X}_{i+1,l} + \gamma^{i,k} \quad (\text{B13})$$

with which we can start a new strike  $i + 1$  up to  $i = N_r$ , which corresponds to the stellar surface. At the surface we require the Lagrangian pressure perturbation  $\delta P$  to vanish and the radial flux perturbation to fulfill Stefan-Boltzmann's relation. In this way  $\mathbf{X}_{N_r+1,j}$  can be ignored, so that the first summation on the right hand side of relations (B9, B10) and equation (B11) vanishes. After working through the last strike  $i = N_r$  we finally arrive at  $j = N_\theta$ . Note that now also the second summation in the above relations has vanished. Substituting the thus simplified relations (B9-B10) and applying the equatorial symmetry relations, all terms in the FDE can now be collected in  $B_2$  and  $D$  only

$$B_2 \mathbf{X}_{N_r, N_\theta} + D = 0 \quad (\text{B14})$$

Solving this equation we find the first perturbation vector  $\mathbf{X}_{N_r, N_\theta} = -B_2^{-1} D$ . We can find all other perturbation vectors by stepping back through the entire elimination procedure. E.g. having solved  $\mathbf{X}_{N_r, N_\theta}$ ,  $\mathbf{X}_{N_r, N_\theta - 1}$ , ...,  $\mathbf{X}_{N_r, j+1}$ , we find  $\mathbf{X}_{N_r, j}$  by direct substitution into the stored relations (B12)

$$\mathbf{X}_{N_r, j} = \alpha^{N_r, j} \mathbf{X}_{N_r, j+1} + \sum_{l=j+2}^{N_\theta} \beta_l^{N_r, j} \mathbf{X}_{N_r, l} + \gamma^{N_r, j} \quad (\text{B15})$$

Having solved in this way for all  $\mathbf{X}_{N_r, l}$ , we find  $\mathbf{X}_{N_r - 1, l}$  from relations (B13), etc.